

RESEARCH ARTICLE

10.1029/2018JD029528

Key Points:

- A pronounced increase of offshore rainfall was observed at southern Hainan in the summer of 2010
- Coastal upwelling was suppressed by southeasterly wind anomalies in the summer of 2003, 2010, and 2016
- Warm SST anomalies due to weak upwelling produces a stronger land breeze and convergence over the sea, ultimately leading to more rainfall

Correspondence to:

D. Wang,
dxwang@scsio.ac.cn

Citation:

Shi, R., Cai, Q., Dong, L., Guo, X., & Wang, D. (2019). Response of the diurnal cycle of summer rainfall to large-scale circulation and coastal upwelling at Hainan, South China. *Journal of Geophysical Research: Atmospheres*, 124, 3702–3725. <https://doi.org/10.1029/2018JD029528>

Received 21 AUG 2018

Accepted 21 FEB 2019





Accepted article online 1 MAR 2019

Published online 3 APR 2019

Author Contributions:

Conceptualization: Rui Shi**Data curation:** Qinbo Cai, Lingyu Dong**Supervision:** Dongxiao Wang**Writing - original draft:** Rui Shi**Writing - review & editing:** Rui Shi, Xinyu Guo

Response of the Diurnal Cycle of Summer Rainfall to Large-Scale Circulation and Coastal Upwelling at Hainan, South China

Rui Shi¹ , Qinbo Cai^{2,3} , Lingyu Dong⁴, Xinyu Guo⁵ , and Dongxiao Wang^{1,6} 

¹State Key Laboratory of Tropical Oceanography, South China Sea Institute of Oceanology, Chinese Academy of Sciences, Guangzhou, China, ²Key Laboratory of South China Sea Meteorological Disaster Prevention and Mitigation of Hainan Province, Haikou, China, ³Hainan Meteorological Service, Haikou, China, ⁴Hainan Meteorological Observatory, Haikou, China, ⁵Center for Marine Environmental Studies, Ehime University, Matsuyama, Japan, ⁶Guangzhou Branch, University of Chinese Academy of Sciences, Beijing, China

Abstract The modulation of coastal rainfall at Hainan by large-scale circulation and coastal upwelling is studied using observations and numerical modeling. Tropical Rainfall Measuring Mission data show that the monthly mean rainfall off southern Hainan was considerably higher in August 2010 than in August 2011. The main cause of this difference is an intensification of offshore rainfall from midnight to early morning. Compared with the multiyear (2000–2017) average field, reanalysis data show that there is an apparent increase in atmospheric humidity in August 2010. During this time, a moderate El Niño was decaying and a new La Niña event was developing, so a significant adjustment of the large-scale circulation was observed in the western Pacific. The resulting anomalous onshore wind depresses the development of upwelling, leading to a relatively warm sea surface temperature off the south coast of Hainan, which in turn enhances the land-sea thermal contrast and land breeze at night. Decreases in upwelling intensity and asymmetric intensification of nocturnal and daytime offshore rainfall are confirmed not only in the summer of 2010 but also in the summer of 2003. Numerical simulations using the Weather Research and Forecasting model verify that the enhanced land breeze ultimately leads to pronounced coastal rainfall off southern Hainan at night. The results indicate that localized surface convergence associated with the sea and land breezes may be more important than the atmospheric humidity and convective instability in modulating the diurnal cycle of rainfall for tropical islands.

1. Introduction

Precipitation on tropical and subtropical islands has a pronounced diurnal cycle that appears as a systematic phase shift between the island and its surrounding sea. The rainfall over the island starts near its coastline in the afternoon and quickly reaches its peak in the early night. Around midnight, the rainfall moves from the land to the surrounding water, reaching a peak in the early morning before dissipating around noon. This phenomenon has been frequently documented for the Maritime Continent region, via surface observations (Houze et al., 1981; Johnson & Priegnitz, 1981; Kamimera et al., 2012; Kanamori et al., 2013), satellite observations (Ichikawa & Yasunari, 2006; Keenan & Carbone, 2007; Kikuchi & Wang, 2008; Nesbitt & Zipser, 2003; Williams & Houze, 1987; Yamamoto et al., 2008; Yang & Slingo, 2001), and numerical simulations (Love et al., 2011; Sato et al., 2009).

In the tropics, the diurnal cycle of rainfall is considered as a key process in the variability of rainfall not only on the diurnal scale itself but also on the synoptic, intraseasonal, and seasonal scales (Birch et al., 2016; Ichikawa & Yasunari, 2006; Koh & Teo, 2009; Peatman et al., 2014; Seo et al., 2014; Slingo et al., 2003; Vincent & Lane, 2016). However, the processes regulating the diurnal cycle of precipitating systems over tropical islands are complicated and poorly understood. Factors to consider, both individually and together, include sea and land breezes (Houze et al., 1981; Love et al., 2011; Miller et al., 2003; Sato et al., 2009; Wapler & Lane, 2012), propagating gravity waves generated by convective instability (Kilpatrick et al., 2017; Mapes et al., 2003; Yokoi et al., 2017), and upslope flows due to obstacles. Crucially, these processes are believed to be significantly influenced by the characteristics of the coastal ocean. Thus, greater knowledge of the influence of oceanic processes on the diurnal cycle of rainfall will improve our understanding of multiscale interactions in tropical and subtropical regions.

The mesoscale structures of sea surface temperature (SST) associated with upwelling or fronts potentially influence the diurnal cycle of rainfall. Observational and numerical studies have shown that mesoscale SST variations associated with fronts and eddies result in mesoscale variations in sea surface winds, cloud formation, and rainfall (Chelton, 2013; Czaja & Blunt, 2011; Kuwano-Yoshida & Minobe, 2017; Minobe et al., 2008; Nakamura et al., 2012; O'Neill et al., 2010; Perlin et al., 2014; Seo, 2017; Small et al., 2008; Tanimoto et al., 2009; Xu et al., 2011). This is because the response of surface wind to mesoscale SST structures can modify the surface convergence field, which is considered to play a fundamental role in convective systems and rainfall (Kilpatrick & Xie, 2015; Mapes et al., 2009; Zipser, 1977). Previous studies have carefully examined this air-sea interaction between coastal upwelling and surface winds (Boé et al., 2011; Perlin et al., 2007), whereas related research on the diurnal cycle of rainfall has been limited.

The South China Sea (SCS) is an epicontinental marginal sea linking the western Pacific Ocean and eastern Indian Ocean (Figure 1a). The interaction between the basin gyre, monsoon, bathymetry, and tide generates mesoscale oceanic processes, such as upwelling, fronts, and eddies, in the northern SCS (NSCS) throughout the year (Chu & Wang, 2003; Hu et al., 2003; Shi et al., 2015; Wang et al., 2001). The influence of ocean fronts and eddies on wind has been investigated in the NSCS region, and the major conclusions from these studies are consistent with the positive correlation between SST and wind in the open ocean (Chow & Liu, 2012; Shi et al., 2017; Wang et al., 2012). A connection between ocean fronts and rainfall was also reported by Toy and Johnson (2014), who found that modification of the convergence and water vapor transport by SST fronts can significantly change the spatial distribution of rainfall.

In summer, several coastal upwelling systems are identifiable in the northwestern SCS through observations of low SST and high chlorophyll concentrations, associated with the dominant southwesterly monsoon. The dynamical mechanism and biogeochemical effects of these upwelling systems have been described for the coastal regions of Guangdong Province, the Taiwan Strait, and eastern Vietnam (Gan et al., 2009; Hu et al., 2001; Shu et al., 2011; Wang et al., 2014; Xie et al., 2003). Su and Pohlmann (2009) and Jing et al. (2015) studied the upwelling and upwelling-induced thermal fronts around Hainan (Figure 1b) using satellite measurements and hydrological surveys. They concluded that the spatiotemporal characteristics of the upwelling are strongly regulated by wind forcing, meaning that the annual variations in upwelling are highly sensitive to changes in the large-scale circulation. Their studies documented the atmospheric influences on the upwelling system at Hainan; however, the feedback of this upwelling to local rainfall, especially its diurnal variation, needs further study.

The diurnal cycle of rainfall in the SCS and southern China regions has been documented previously (Chen et al., 2013; Mao & Wu, 2012) in studies that noted the apparent diurnal variation of rainfall in coastal areas, although their major conclusions emphasized the influence of large-scale topography and monsoonal variability. In the present study, the local effect of coastal upwelling on the diurnal cycle of rainfall at Hainan is investigated using observations and numerical simulations. The analysis focuses on 2 months of data for August 2010 and 2011 because an anomalous increase in offshore rainfall was observed at southern Hainan in 2010, in sharp contrast to the reduced rainfall in 2011. A detailed investigation is required to determine whether the significant change in rainfall intensity was caused by a change in atmospheric circulation or by the regulation of coastal oceanic processes. The remainder of the paper is organized as follows. Section 2 introduces the data and model, and the observed changes in the diurnal rainfall cycle are presented in section 3. The change in synoptic conditions and coastal upwelling in 2010–2011 are analyzed in sections 4. As 2010 was the decaying summer of an El Niño event, we also look at three other El Niño events after 2000 in section 5. The results from the numerical simulation are presented in section 6. Finally, a summary of the key findings is provided in section 7.

2. Data and Methods

2.1. Radar and Rainfall Data

We use monthly radar reflectivity data from the Hainan Meteorology Administration, China. The meteorological radar operates at 2700–3000 MHz and the accuracy of observation is 1 dBZ. The spatial resolution of the observed reflectivity is 1 (2) km within a detecting radius of 230 (460) km. To further diagnose the activity of rainfall systems, we use the real-time rainfall product (3B42RT, version 7) of the Tropical Rainfall Measuring Mission (TRMM). This product is a combination of data observed by multiple passive

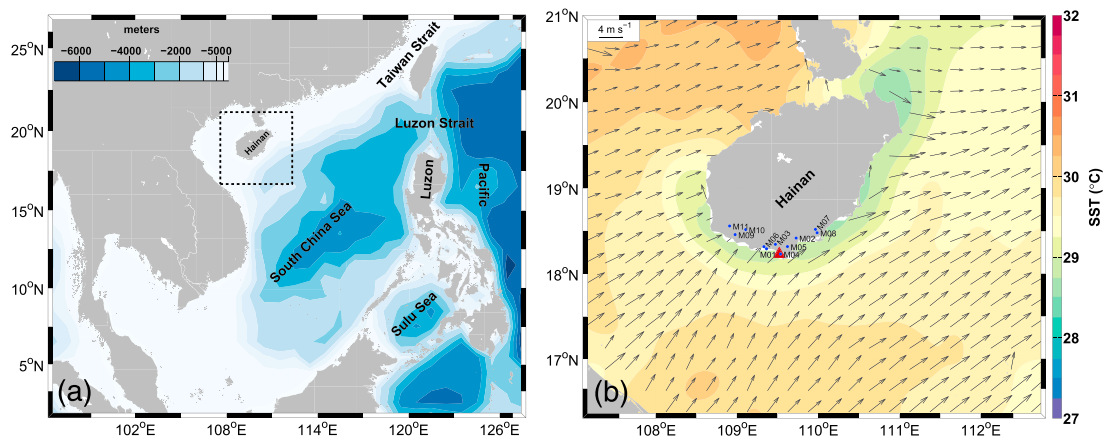


Figure 1. (a) Map of the South China Sea and surrounding area, shading shows bathymetry; (b) monthly mean sea surface temperature (SST; color shading, °C) and sea surface wind (vectors, m/s) averaged for August from 2000 to 2017. The entire area in (a) is the outer domain of the numerical simulation with a resolution of 15 km, and the black rectangle in (a) denotes the inner domain with a resolution of 3 km. The red triangle in (b) is the location of Sanya station for radiosonde observations. Blue dots indicate the 11 automatic weather stations.

microwave sensors, including the TRMM Microwave Imager, the Special Sensor Microwave Imager, the Advanced Microwave Scanning Radiometer, and the infrared data observed by geosynchronous satellite. The 3B42RT data cover the period from 2000 to the present. The 3B42RT data have a high spatial (0.25°) and temporal (3-hr) resolution and so are widely used to study the fine-scale features and diurnal cycle of rainfall in tropical areas (Kikuchi & Wang, 2008; Sahany et al., 2010).

2.2. SST and Wind Data

Data from the Operational SST and Sea Ice Analysis (OSTIA) are used to investigate the variation in upwelling at Hainan. These data are produced by the U.K. Met Office with support from the My Ocean project. The OSTIA system makes extensive use of multiple satellite retrievals and assimilates in situ observations from the Global Telecommunications System to generate a global daily SST map with (1/20)° (~6-km) resolution since 2006. It is currently used operationally as the boundary condition for all weather forecast models at the U.K. Met Office and European Centre for Medium-Range Weather Forecasts (Donlon et al., 2012). The high accuracy and resolution of OSTIA data can be helpful in simulating the influence of mesoscale SST perturbations on the sea surface wind (O'Neil et al. 2010; Song et al., 2009), so it is used as the bottom boundary condition for the atmospheric model in this study. The sea surface wind data observed by Quick Scatterometer (QuikSCAT) and Advanced Scatterometer (ASCAT) are used in this study. QuikSCAT provides a more extensive geographical and temporal coverage and higher spatial resolution of the ocean vector winds since 1999. After QuikSCAT finished its mission in October 2009, ASCAT continues to provide global sea surface wind data. These two kinds of wind data provide a continuous observation of sea surface wind over the SCS.

2.3. Radiosonde and Automatic Weather Station Data

The radiosonde data and automatic weather station (AWS) data are provided by the Hainan Meteorology Administration, China. Seven years of data from 2008 to 2014 are used in this study. The radiosonde observations include pressure, geopotential height, temperature and dew point temperature, and wind direction and speed. They are available at standard pressure levels from 1,000 to 200 hPa. In this study, the radiosonde observations at Sanya station are analyzed because this is the closest station to the southern coastline of Hainan. In addition, the surface observations at 11 AWSs (Figure 1b) close to the coastline are used to validate the numerical simulation results, especially for the simulation of sea and land breezes. The AWSs are within 30 km of the coast, so the climatological mean wind hodographs of these AWSs show an apparent diurnal cycle of sea and land breezes in August.

2.4. Model Configuration

The numerical simulations are carried out using version 3.9 of the Advanced Research version of the Weather Research and Forecasting (WRF) model (Skamarock, 2008) under a two-way nested configuration with horizontal resolutions of 15 and 3 km. The fine-resolution domain focuses on Hainan in the northwestern SCS (Figure 1a). Topography is interpolated from the Global Multi-resolution Terrain Elevation Data (2010) distributed by the U.S. Geological Survey. The vegetation field is interpolated from the Combined Fraction of Photosynthetically Active Radiation and the land category from the 21-class category land use data derived from Moderate Resolution Imaging Spectroradiometer data. Both domains are initialized by European Centre for Medium-Range Weather Forecasts interim reanalysis (ERA-Interim) data at a resolution of $0.75^\circ \times 0.75^\circ$ (Dee et al., 2011). The lateral boundary conditions for the large domain are updated by ERA-Interim data every 6 hr to allow large-scale synoptic weather systems outside of the domain to propagate through the domain. The soil temperature and moisture data used in the simulation are from the National Centers for Environmental Prediction FNL (Final) Operational Global Analysis data ($1^\circ \times 1^\circ$).

The simulations are performed using 60 vertical sigma levels, including 25 levels below 1,000 m. A fine vertical resolution is specified in the boundary layer to accurately simulate the vertical turbulent momentum exchange in this layer. The Mellor-Yamada-Nakanishi-Niino planetary boundary layer scheme (Nakanishi & Niino, 2006), the Noah land surface model (Chen & Dudhia, 2001), the Dudhia shortwave radiation scheme (Dudhia, 1989), and a rapid radiative transfer longwave radiation scheme (Mlawer et al., 1997) are set for both domains. The new Tiedtke (Tiedtke, 1989; Zhang et al., 2011) cumulus scheme and the WRF Single-Moment 6-Class Microphysics Scheme (Hong & Lim, 2006) are set for the coarse domain (15 km). In the fine-resolution domain (3 km), the cumulus scheme is turned off and only the microphysics scheme is retained, for better representation of organized convection at a finer resolution. A 1-month simulation is carried out as a sequence of 3-day integrations with an update of the initial conditions by ERA-Interim data after 3 days and then a restart for the following 3-day integration. The SST and soil data are reinitialized at 0000 UTC for each 3-day integration.

3. Rainfall Difference Between 2010 and 2011

3.1. Monthly Mean Reflectivity and Rainfall

The radar observations show an apparent change in the spatial pattern of reflectivity at Hainan between August 2010 and 2011. In August 2010, the meteorological radar observed two high-reflectivity bands (Figure 2a): one over the northern part of the island with reflectivity around 300 dBZ and the other off the southern coastline of Hainan with reflectivity around 200 dBZ. In contrast, only one main high-reflectivity band is observed in the central area of Hainan in August 2011, and the reflectivity is higher over the western (550 dBZ) than the eastern (300 dBZ) area (Figure 2b). The high-reflectivity band off the southern coast of Hainan observed in 2010 almost disappears in 2011.

The radar echo maps indicate where convective systems occur, frequently in association with rainfall. As presented in Figure 2, the merged satellite rainfall data (3B42RT) and radar data match closely, providing a reliable snapshot of the convective activity in August 2010 and 2011 (Figures 2c and 2d). In August 2010, two major rainfall bands are apparent over the northern land area and southern ocean area off Hainan (Figure 2c; $17.5\text{--}18.3^\circ\text{N}$, $108.5\text{--}110.5^\circ\text{E}$), coinciding almost exactly with the areas showing strong radar echoes. However, the width of the rainfall band off the southern coast seems wider than the high-reflectivity band. The maximum rainfall rates of these two major rainfall bands are almost the same, at about 0.6 mm/hr. The rainfall rate over most of the ocean region exceeds 0.25 mm/hr, except to the northeast of Hainan. In August 2011, there is an abrupt weakening of reflectivity and rainfall, especially off the southern coast of Hainan (Figure 2d). The intensity of rainfall over the sea falls below 0.15 mm/hr and the rainfall band over land shifts to the central area of the island.

The significance level of the rainfall anomaly in 2010 and 2011 is then examined using the climatological mean over 18 years from 2000 to 2017. The climatological mean rainfall in August is mostly concentrated over land, with the rainfall near the southern coastline being relatively weak (Figure 3a). The rainfall rate off the southern coast of the island in August 2010 is almost twice the 18-year mean (0.50 vs. 0.25 mm/hr), making it apparent positive anomalies that pass the 95% significance test (black dashed contour in Figure 3b). Negative anomalies in rainfall rate occur over the whole study area in 2011,

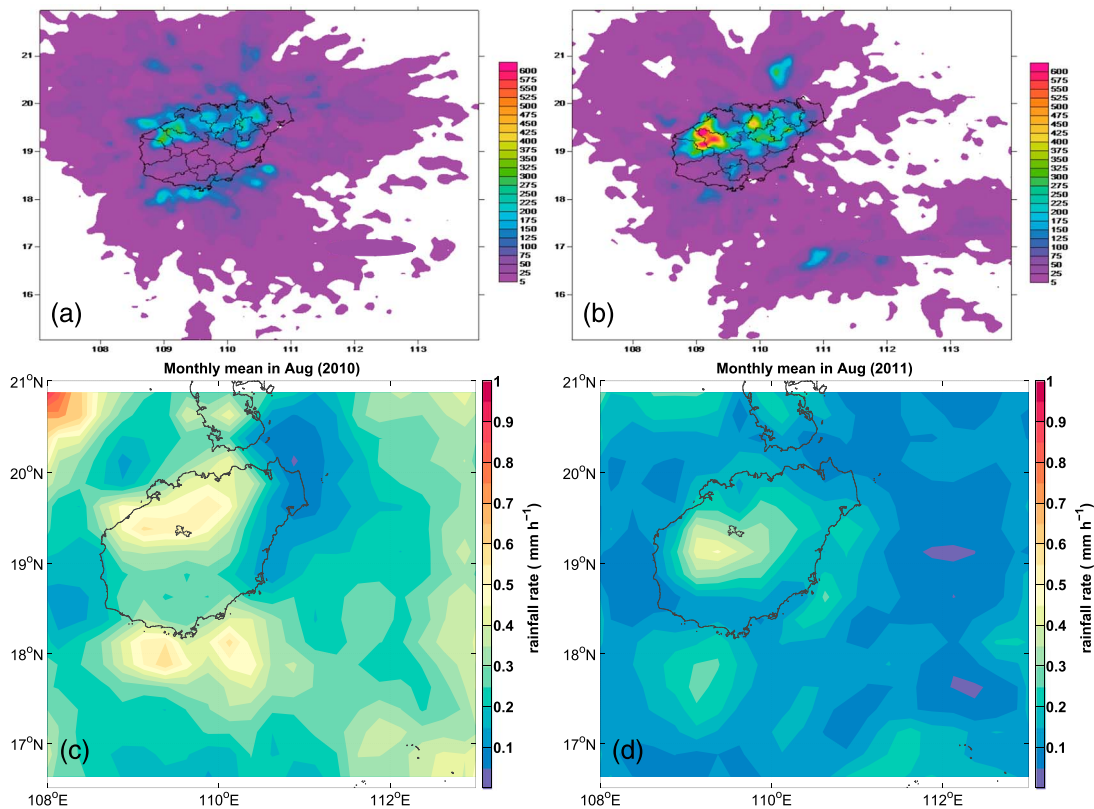


Figure 2. (a) Monthly mean reflectivity (dBZ) observed by meteorological radar in August 2010. (b) Observed reflectivity in August 2011. (c) Monthly mean rainfall rate (mm/hr) derived from the Tropical Rainfall Measuring Mission 3B42RT dataset in August 2010. (d) The same as (c) but in August 2011.

but their magnitude does not pass the significance test (Figure 3c). Thus, the positive anomaly in rainfall off the southern coastline of Hainan in August 2010 is rare, warranting further study.

3.2. Diurnal Cycle of Rainfall

Since the monthly mean rainfall shows a significant enhancement off the southern coast of Hainan in August 2010, this variation might also be imprinted on the diurnal cycle of rainfall. Thus, the diurnal evolutions of the monthly mean of the 3-hourly interval rainfall rate are shown in Figure 4. A shift in the diurnal cycle of rainfall between the land and the surrounding sea of Hainan is evident in 2010 (Figure 4a). Nocturnal rainfall appears over the southern part of the island and in the offshore area after 2300 LST (15 UTC). The extent and strength of the offshore rainfall reach their maximum values in the early morning and the rainfall gradually dissipates before 1100 LST. Conversely, rainfall over land starts over the northern part of the island in the early afternoon (1400 LST). It moves slowly southward to the central and southern areas of the island and reaches its maximum before 1700 LST. The rainfall over land dissipates before 2000 LST and a clear sky is observed over land throughout the night. In August 2011, there is a significant reduction in the extent and magnitude of the offshore rainfall compared with the diurnal cycle of rainfall in August 2010 (Figure 4b). The nocturnal rainfall band disappears off the southern coast of Hainan, and only a small area of rainfall is observed before 0800 LST. The rainfall over land is also weaker in 2011 than in 2010 before 17 LST, especially in the northern Hainan. In addition, the rainfall over land persists until 2000 LST in 2011 that is a longer than in 2010 (Figure 4c).

To quantify the contribution of the change in the diurnal cycle of rainfall to the monthly mean anomaly, the occurrence frequency and intensity of rainfall are calculated over the area of significant anomalies shown in Figure 3b. Compared with the August climatological mean, the frequency and intensity of nocturnal rainfall both increased in 2010 (Figures 5a and 5b). The average number of offshore rainy days is less than 12 days, but it sharply increased to 22 days in 2010 (Figure 5a). In addition, the nocturnal rainfall rate increased to

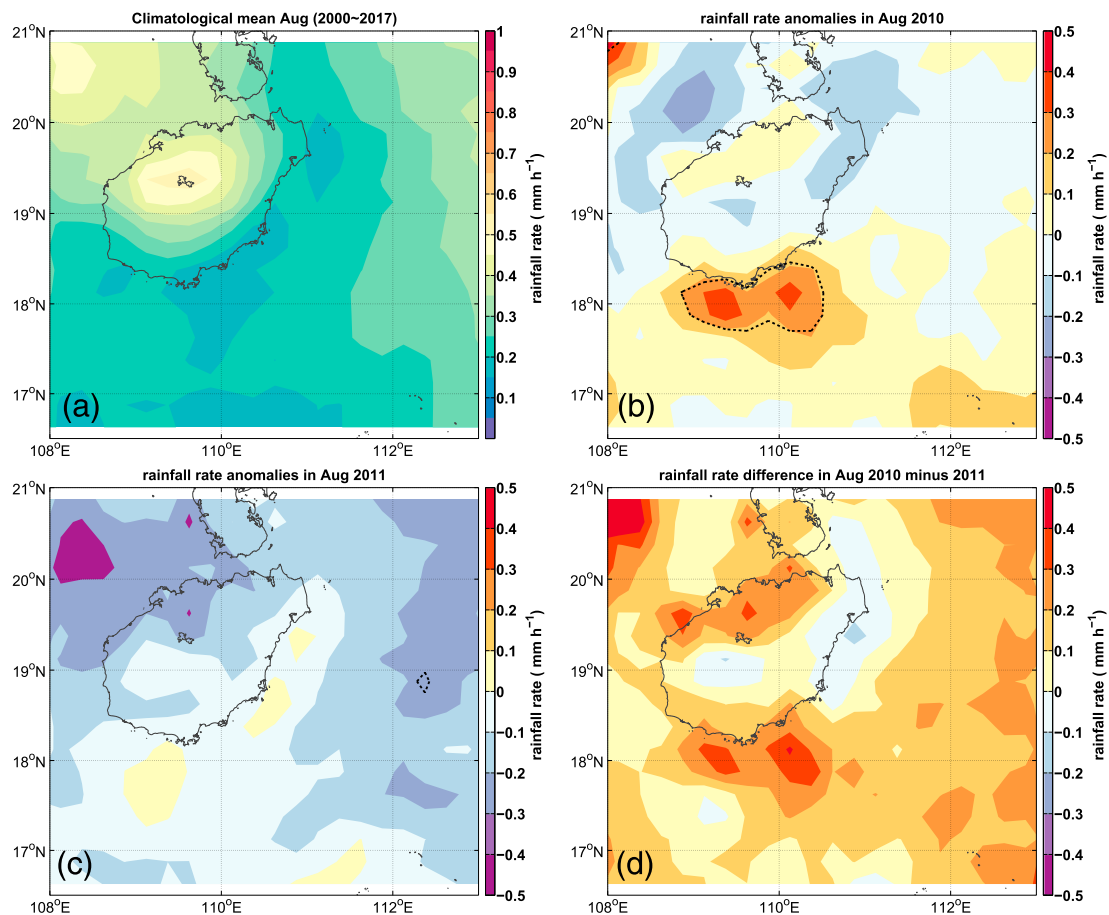


Figure 3. (a) Climatological rainfall rate (mm/hr) averaged in August from 2000 to 2017 from the Tropical Rainfall Measuring Mission 3B42RT data set. (b) Anomalies (mm/hr) for August 2010. (c) The same as (b) but for August 2011. (d) The difference between August 2010 and 2011. The black dashed contour in (b) indicates the significance level ($\alpha = 0.05$) of anomalies from the climatological mean.

1.8 mm/hr in 2010 compared with a climatological mean nocturnal rainfall rate of about 1.0 mm/hr (Figure 5b). The peak nocturnal rainfall rate occurred before 0500 LST in 2010, which is 3 hr earlier than the peak of the climatological mean. The average offshore rainfall rate is about 0.5 mm/hr in the afternoon and is not very different in 2010. The total number of rainy days varies a little from the climatological mean in 2011, but the intensity of rainfall is weaker than the average over the whole day.

4. Analysis of the Synoptic Background

The radar and satellite observations show an apparent change in monthly mean rainfall at Hainan in August 2010, especially in the nearshore area off the southern coastline. Moreover, this change seems to be related to the markedly higher offshore rainfall in the night and early morning. Previous studies have reported that several processes are closely related to the occurrence and migration of nocturnal offshore rainfall near tropical islands, such as large-scale circulation, and sea and land breezes (Houze et al., 1981; Wapler & Lane, 2012). In this section, the influence of the synoptic background variation is analyzed.

4.1. Variation in Large-Scale Circulation

According to the Oceanic Niño Index (ONI) distributed by NOAA (http://origin.cpc.ncep.noaa.gov/products/analysis_monitoring/ensostuff/ONI_v5.php), an El Niño event occurred from 2009 to 2010 and was followed by a strong La Niña event. The previous studies have documented El Niño–Southern Oscillation events have a lagged impact on the SST and regional climate at SCS in the summer of the following year (Du et al., 2009; Hu et al., 2017; Huang et al., 2000; Liu et al., 2014; Wang et al., 2000; Wu et al., 2014; Xie

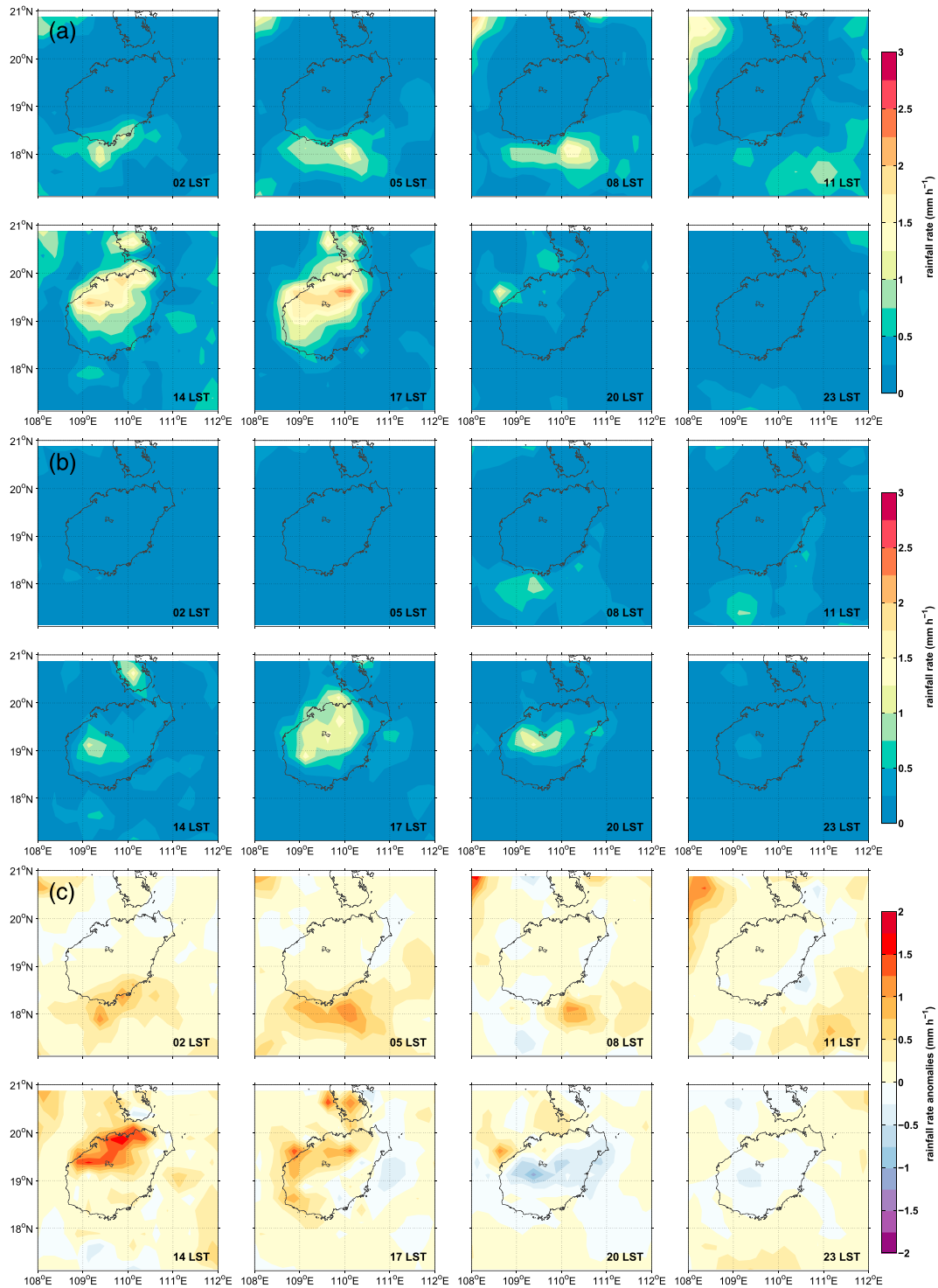


Figure 4. (a) Diurnal cycle of the monthly mean rainfall rate (mm/hr) derived from the Tropical Rainfall Measuring Mission 3B42RT data set at intervals of 3 hr in August 2010. (b) The same as (a) but in August 2011. (c) The differences between 2010 and 2011 (i.e., 2010 minus 2011). The numbers in the bottom right of the subplots show the time (LST).

et al., 2009, 2010; Zhang et al., 2017). The change in atmospheric moisture induced by the variation in large-scale circulation in the SCS may be one possible reason for the anomalous intensification of offshore rainfall in 2010. Therefore, the moisture and thermal structure of the atmosphere are examined using ERA-Interim data on 850 and 500 hPa (Figure 6).

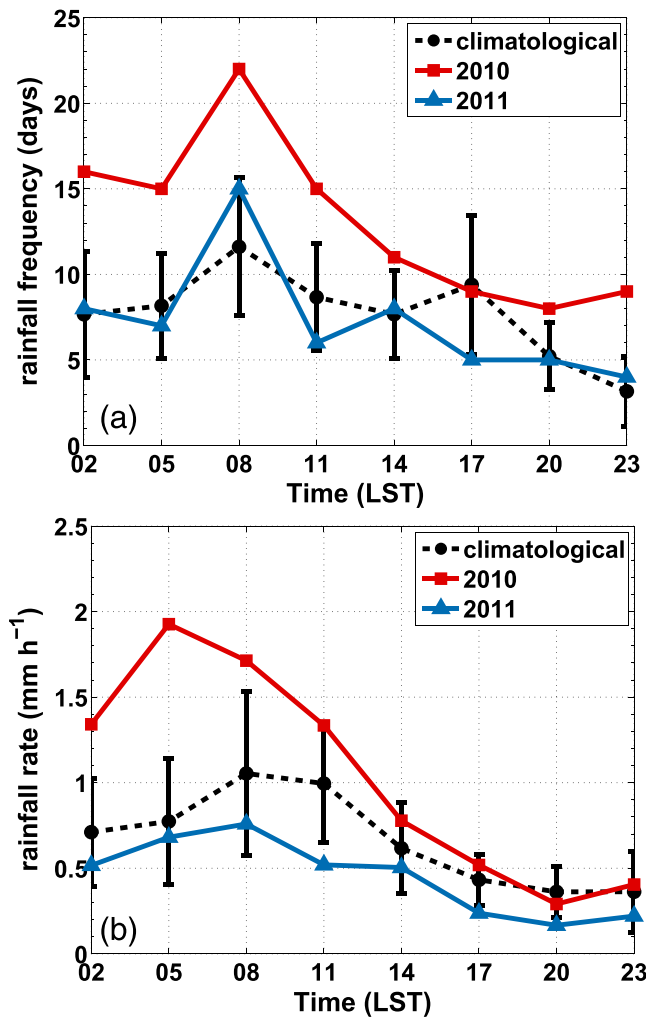


Figure 5. (a) Total rainy days and b intensity of rainfall events in each phase of the diurnal cycle. The rainy days are counted where the rainfall rate is nonzero over the area of significant change shown in Figure 3b, while the intensity of rainfall is a spatial average. The black dashed lines denote the climatological mean with ± 1 standard deviation (vertical bars) from 2000 to 2017. The red and blue lines denote the years 2010 and 2011, respectively.

vapor and produce more convective rainfall. The convective instability of the environment is an important factor when investigating the potential occurrence frequency of rainfall. Therefore, we use the radiosonde observations at Sanya to estimate the height of the lifting condensation level (LCL; h_{lcl}), the convective available potential energy (CAPE), and convective inhibition (CIN). The h_{lcl} is determined from the temperature of the LCL (T_{lcl}), which is calculated following Bolton (1980):

$$T_{lcl} = (1/(T_D - 56) + \ln(T_0/T_D)/800)^{-1} + 56, \quad (1)$$

where T_0 and T_D are the temperature and dew point temperature at 1,000 hPa in kelvins, respectively. Then, the height can be simply estimated as follows:

$$h_{lcl} = (T_{lcl} - T_0)/\gamma + h_{T_0}, \quad (2)$$

where $\gamma = 9.8 \times 10^{-3}$ K/m is the dry adiabatic lapse rate and h_{T_0} is the height of 1,000 hPa. CAPE is calculated by integrating the positive buoyancy for a lifting saturated air parcel from the free convection height h_{lfc} to the equilibrium level h_{el} :

The climatological (2000–2017) average for August has horizontally uniform specific humidity over the SCS, while the northwestern area is higher than the southern area during August (Figures 6a and 6b). The positive anomalies in specific humidity during August 2010 suggest an abundant water vapor supply in the troposphere over the SCS (Figures 6c and 6d), which may have produced more offshore rainfall at Hainan. In contrast, negative anomalies appear over most of the NSCS in August 2011, which suggests reduced humidity and rainfall at Hainan (Figures 6e and 6f). The different wind anomalies at 850 and 500 hPa show the change of atmospheric circulation in August 2010 and 2011. In August 2010, there are easterly wind anomalies in the SCS at 850 and 500 hPa, and the easterly wind anomalies change to southeasterly near Hainan (Figures 6c and 6d). In 2011, the 850-hPa wind anomalies become very weak and even disappear near Hainan (Figure 6e). At 500 hPa, an anomalous anticyclone located over the Indochina Peninsula and NSCS produces southeasterly wind anomalies over southern Hainan (Figure 6f).

As a supplement to the ERA-Interim reanalysis data, we also examine radiosonde observations from Sanya station (red triangle in Figure 1b) located on the southern coast of Hainan, where atmospheric conditions are expected to be similar to the offshore area. The monthly mean profiles show that the specific humidity varies little (Figures 7a and 7b), but the relative humidity varies substantially (Figures 7c and 7d). The diurnal variation in humidity is also small, although the relative humidity is slightly higher in the early evening than in the morning (Figures 7c and 7d). In 2010, the relative humidity anomaly with respect to the multiyear average is positive from the surface to about 450 hPa but negative in the upper air. In 2011, both specific humidity and relative humidity are lower than the multiyear average from the surface all the way through to the upper air. Therefore, the radiosonde observations are further evidence for the significant variation in atmospheric humidity near Hainan in 2010 and 2011. However, the temperature profiles for the 2 years show little difference from the multiyear average (Figure 8).

4.2. Variation in Convective Instability

The anomalous wet conditions in 2010 seen in the reanalysis and radiosonde data require further discussion of the processes that release water

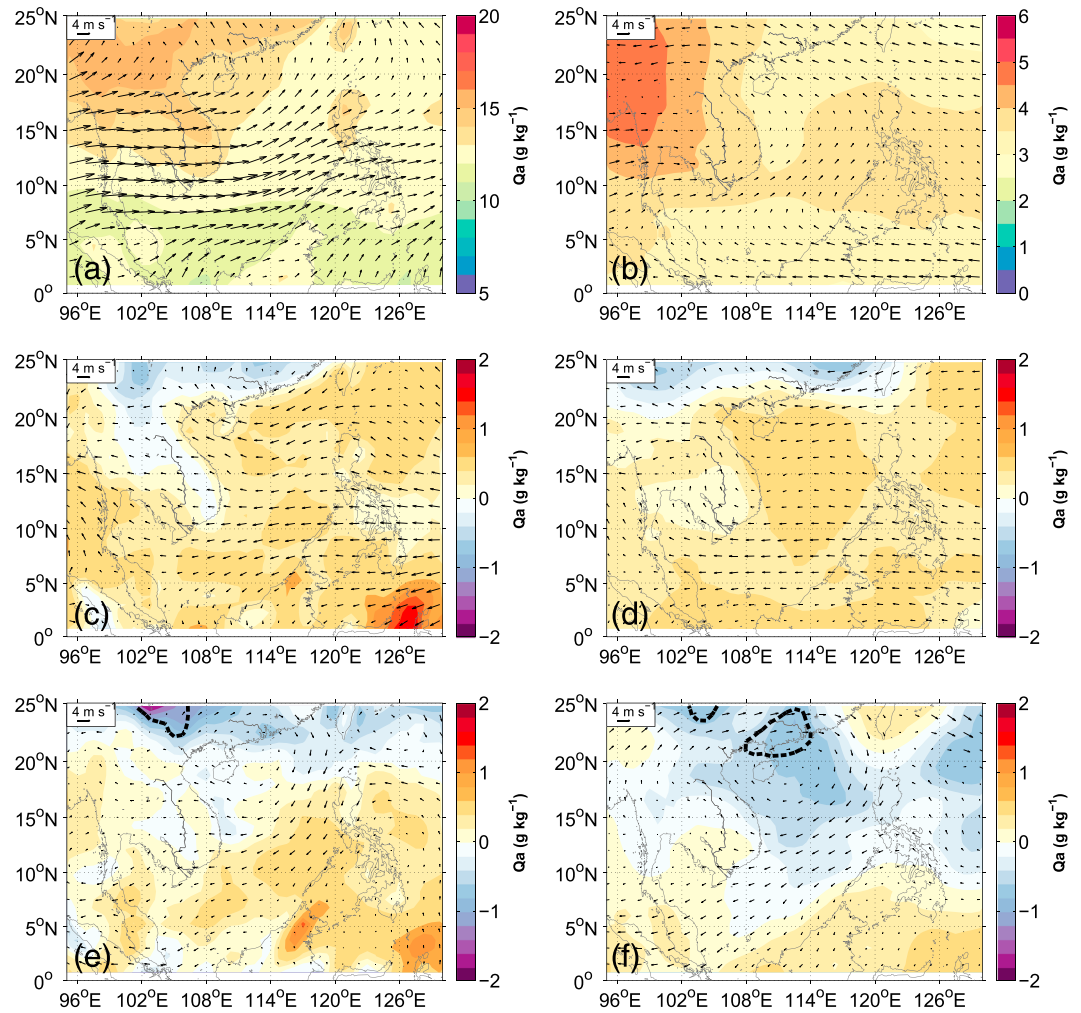


Figure 6. Monthly mean specific humidity (color shading, g/kg) and wind (vectors, m/s) at 850 hPa (left column) and 500 hPa (right column) from European Centre for Medium-Range Weather Forecasts interim reanalysis data. The top panels (a, b) show the climatological mean from 2000 to 2017; the middle panels (c, d) show the anomalies in August 2010; and the bottom panels (e, f) show the anomalies in August 2011. The black dashed contour in (e) and (f) indicates the significance level ($\alpha = 0.05$) of anomalies. Note the different color bars for (a) and (b).

$$\text{CAPE} = \int_{h_{\text{lic}}}^{h_{\text{el}}} g \left(\frac{T_{v,\text{parcel}} - T_{v,\text{env}}}{T_{v,\text{env}}} \right), \quad (3)$$

where $T_{v,\text{parcel}}$ and $T_{v,\text{env}}$ are the virtual temperatures of a specific air parcel and the environment, respectively, and g is the gravitational constant.

Estimates of the convective parameters are given in Table 1. In general, the atmosphere is nearly convectively unstable at Hainan in summer, and the CAPE is larger in the early night (2000 LST) than in the morning (0800 LST; Table 1). The LCL is below 500 m in the early morning but increases by about 200 m at night. Since the atmosphere is warm and wet near the sea surface (Figures 7 and 8), the value of CIN is small over the whole day (Table 1). In general, the LCL height is lower in 2010 than in 2011 (Table 1), which means a lifted air parcel will reach saturation more easily in 2010 than in 2011. The monthly mean CAPE, which is determined by the area enclosed between the temperature and saturation-adiabatic lifting trajectories upon LCL is around 2.0×10^3 J/kg, indicating that the coastal atmosphere is convectively unstable most of the time. The CAPE is not very different in August 2010 and 2011, though it is even lower in 2010 than in 2011. This suggests that the atmosphere is more convectively unstable in 2011 than 2010 at the time of observation, possibly because of the drier and colder upper air in 2011 (Figures 7 and 8), which led to

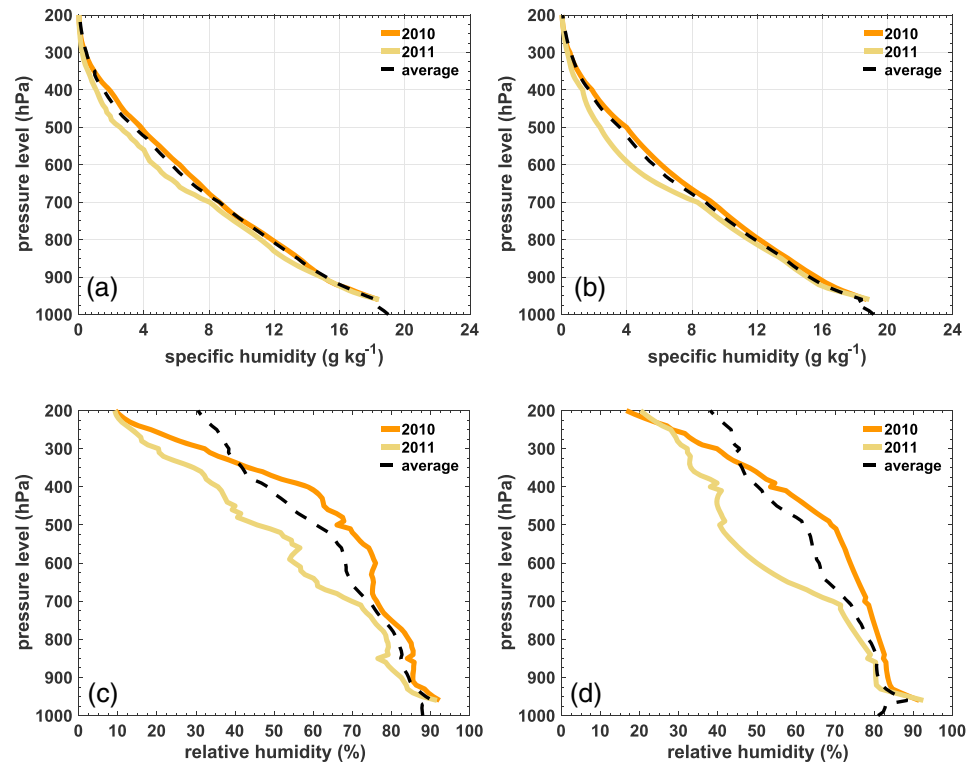


Figure 7. (a, b) Monthly mean specific humidity (g/kg) and (c, d) relative humidity (%) profiles observed at Sanya station. The black dashed lines are the multiyear average from 2008 to 2014. The orange and green heavy lines denote the values for 2010 and 2011, respectively. The observation time is 0800 LST for the left-hand column and 2000 LST for the right-hand column.

larger CAPE in 2011 than in 2010. Another reason is that heavier rainfall will release more CAPE, so the CAPE is smaller in 2010 than in 2011, especially in the early morning (0800 LST 2010, $1.82 \times 10^3 \text{ J}/\text{kg}$ in Table 1).

The significant enhancement in atmospheric moisture in 2010, as shown by the ERA-Interim data, is clearly shown on the Skew-T map. Thus, the dew point depression in 2010 is much smaller than in 2011.

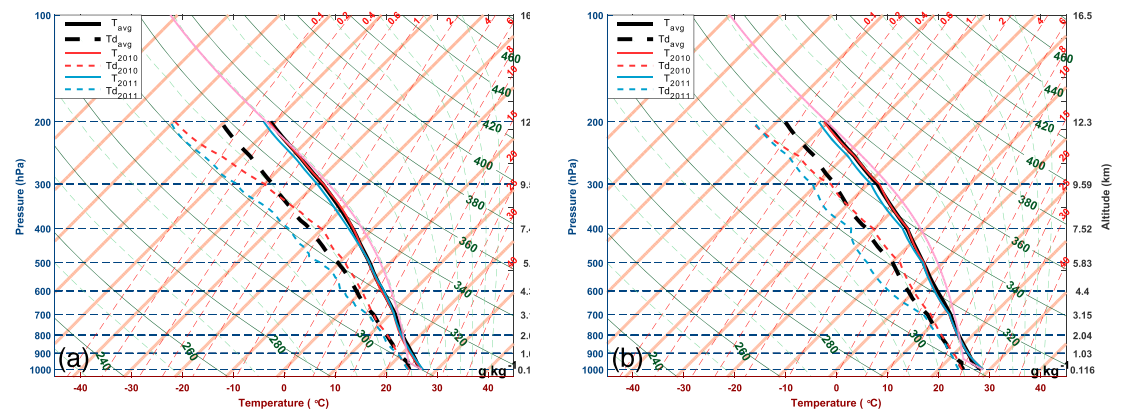


Figure 8. (a) Skew-T map derived from radiosonde observations at Sanya station at 0800 LST; (b) Skew-T map at 2000 LST. The solid lines indicate temperature and the dashed lines indicate dew point temperature. Red and blue colors denote observations in August 2010 and 2011, respectively. Black solid and dashed lines are the mathematical mean of the temperature and dew point temperature profiles in August from 2008 to 2014. The magenta lines denote the dry and saturation-adiabatic lifting trajectories of an idealized air parcel starting from the average profile.

Table 1

Mathematical Mean of the LCL Temperature (T_{lcl}), LCL Height (h_{lcl}), CAPE, and CIN Calculated From the Twice-Daily Radiosonde Observations in August 2010 and 2011 at Sanya

| Year\Time | T_{lcl} (K) | | h_{lcl} (m) | | CAPE ($\times 10^3 \text{ J kg}^{-1}$) | | CIN (J kg^{-1}) | |
|-----------|---------------|--------|---------------|--------|--|-----------------|----------------------------|-------------------|
| | 08 LST | 20 LST | 08 LST | 20 LST | 08 LST | 20 LST | 08 LST | 20 LST |
| 2010 | 296.48 | 296.26 | 451.68 | 667.72 | 1.82 ± 0.57 | 2.14 ± 0.57 | 8.44 ± 15.78 | 9.25 ± 12.00 |
| 2011 | 296.37 | 295.50 | 501.01 | 742.66 | 2.18 ± 0.82 | 2.36 ± 0.69 | 10.68 ± 0.82 | 10.74 ± 9.80 |
| Mean | 297.05 | 296.91 | 484.80 | 671.63 | 2.00 ± 0.78 | 2.26 ± 0.76 | 15.46 ± 0.78 | 17.09 ± 13.10 |

Note. The standard deviation (numbers after “ \pm ”) is also shown for CAPE and CIN. The mean values are calculated over 7 years from 2008 to 2014. Note the different units for CAPE and CIN. CAPE = convective available potential energy; CIN = convective inhibition; LCL = lifting condensation level.

Nonetheless, the difference in atmospheric moisture does not produce a very large change in CAPE between 2010 and 2011. This may be because the positive CAPE is integrated upward from h_{lcl} , which is mainly set by the surface air temperature and humidity (equations (1) and (2)). These two parameters are not very different in 2010 and 2011, so the CAPE is also similar. The monthly mean CAPE is higher at 2000 LST than at 0800 LST, while there is more offshore rainfall at 0800 LST (Table 1). This suggests that the energy available from convective instability does not turn into rainfall immediately but a daily alternative process triggers the releasing of the unstable energy. In other words, lifting processes associated with sea or land breeze may be more important than convective instability in modulating the diurnal cycle of rainfall near the island.

5. Atmospheric Circulation and Coastal Upwelling

5.1. Variation in Surface Wind and Upwelling

The anomalous atmospheric circulation in the summer of 2010 not only changed the humidity of the upper air but also the surface wind and significantly modulated the coastal upwelling near Hainan in 2010. The variation in coastal upwelling appears to have been associated with a change in SST (Figure 9). In 2010, the prevailing southeasterly monsoon dominated the northwestern SCS. The weak alongshore wind is unfavorable for the development of upwelling off southern Hainan, and only weak upwelling is observed along the eastern and western coastal sea (Figure 9a). Since the upwelling of cold water is suppressed, the coastal SST off the southern coastline of the island exceeded 29°C in 2010 (Figure 9a). In contrast, the upwelling system developed fully to the south and east of Hainan in 2011 (Figure 9b). The prevailing wind changed to southerly and southwesterly nearshore, which favored upwelling. Thus, the nearshore SST fell to about 28°C because of the upwelling of cold water (Figure 9b).

The variation in SST due to upwelling resulted in a marked change in the thermal contrast between land and ocean. This led to a corresponding adjustment of sea and land breezes, which is closely related to the diurnal

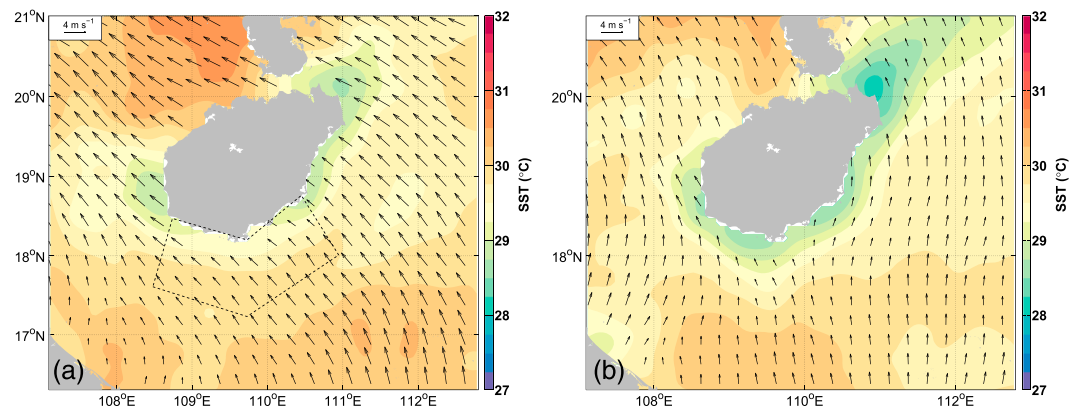


Figure 9. (a) Monthly mean sea surface temperature (color shading, $^\circ\text{C}$) and wind field (vectors, m/s) in August 2010. (b) The same as (a) but in August 2011. The black dashed line in (a) encloses the region over which the upwelling index $UI_{\Delta SST}$, and total offshore rainfall are calculated.

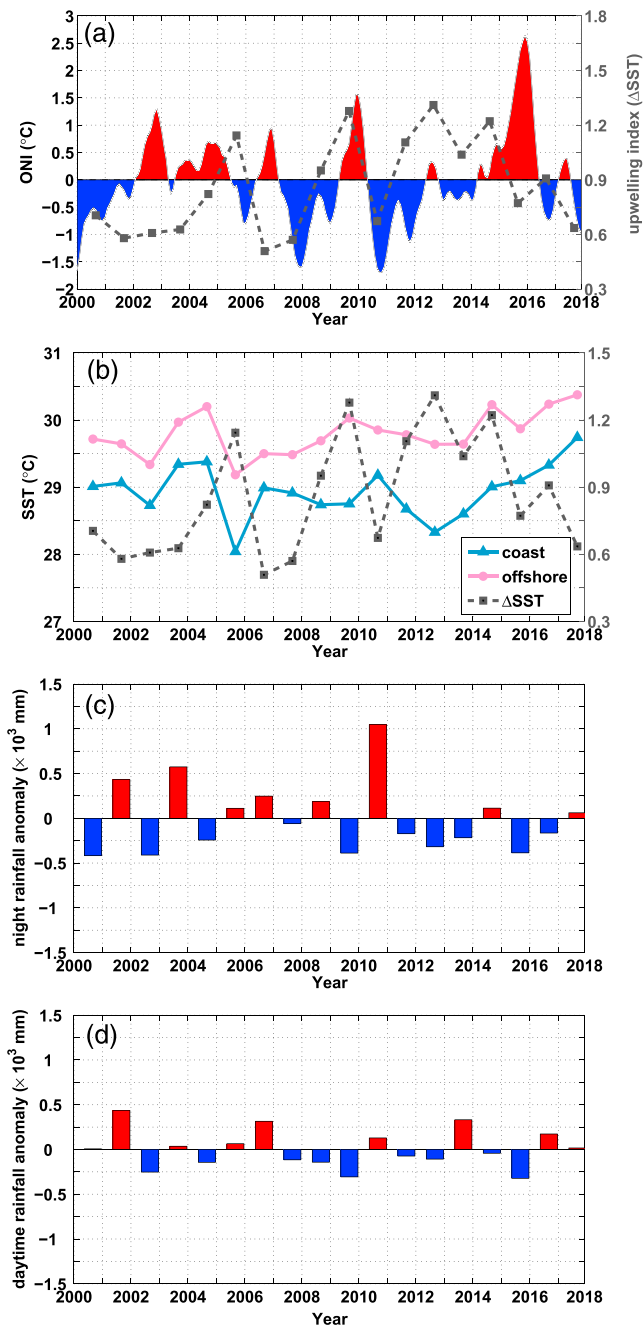


Figure 10. (a) Monthly Oceanic Niño Index (ONI) from National Oceanic and Atmospheric Administration (color shading) and upwelling index $UI_{\Delta SST}$ (gray dashed line) from 2000 to 2017. (b) Upwelling index $UI_{\Delta SST}$ (gray dashed line), sea surface temperature (SST) near coast (blue line), and SST of open ocean (magenta line) from 2000 to 2017. (c) Anomalies in total nocturnal rainfall (0200–0800 LST) for August from 2000 to 2017. (d) The same in (c) but for daytime rainfall (1400–2000 LST). The definition of $UI_{\Delta SST}$ is given in section 6. $UI_{\Delta SST}$ and total rainfall are calculated for the region shown in Figure 9a. Anomalies are calculated as the monthly mean minus the multiyear average from 2000 to 2017.

there are still some uncertainties due to the complexity of El Niño itself. The location of the region of warm SST anomalies in the Pacific defines two types of El Niño: the eastern-Pacific (EP) El Niño and central-Pacific (CP) El Niño (Ashok et al., 2007). The CP El Niño can be further classified into two cases by the

cycle of rainfall on tropical islands. Warmer water near the southern coastline of the island may produce a stronger land breeze at night, leading to the enhanced rainfall in August 2010. Likewise, colder water off the coast of the island may maintain sea breeze in a longer time, leading to more rainfall in the late afternoon. To examine this hypothesis, the correlation between atmospheric circulation and upwelling intensity is further examined for other weak upwelling years.

5.2. Correlation between Upwelling Intensity and Diurnal Cycle of Rainfall

To quantify the variability in upwelling intensity after 2000, an upwelling index $UI_{\Delta SST}$ is defined as the difference in SST between the coast and the ocean, as follows:

$$UI_{\Delta SST} = -(SST_{\text{coast}} - SST_{\text{ocean}}), \quad (4)$$

where SST_{coast} is the average SST of grid cells that are closest to the coastline (offshore distance of <5 km) and SST_{ocean} is the average SST of grid cells that are about 100 ± 5 km from the coastline. Therefore, an increase in $UI_{\Delta SST}$ corresponds to an increase in upwelling intensity.

The upwelling index for the coastal region south of Hainan shows an apparent year-to-year variation in upwelling intensity from 2000 to 2018. The upwelling index is relatively small in the summers of 2003, 2010, and 2016, when the El Niño event is decaying (Figure 10a). The upwelling index $UI_{\Delta SST}$ decreases to about 0.6 in August 2003, which shows a similar depressed upwelling as August 2010 ($UI_{\Delta SST} \approx 0.66$). The upwelling index is 0.9 in August 2016, which is slightly larger than the index values in 2003 and 2010 but is still smaller than the indexes of peak years. Summer 2005 is a different case: The upwelling intensity is comparable to that of normal years, although it is the decaying summer of the 2004/2005 El Niño. In general, the decreases in the upwelling index in 2003, 2010, and 2016 are caused mainly by the increase in coastal SST (~ 29.5 °C), because the correlation coefficient between SST_{coast} and $UI_{\Delta SST}$ is -0.58 , while the correlation coefficient between SST_{ocean} and $UI_{\Delta SST}$ is only 0.10 (Figure 10b).

Then, the correlation between upwelling intensity and the diurnal cycle of rainfall is investigated in 2003, 2006, and 2010. There is clearly an asymmetric modulation of the nocturnal and daytime rainfall by the upwelling in the 2003 and 2010 cases (Figures 10c and 10d). The decrease in upwelling intensity coincides well with a significant increase of nocturnal offshore rainfall, and the strongest effect appears in 2010 (Figures 10a and 10c). At the same time, the weak upwelling does not lead to an apparent increase in daytime rainfall (Figure 10d). This suggests that the land-sea thermal contrast, modified by the upwelling, has different effects on the sea and land breeze circulation, which may then regulate the convective rainfall during daytime and night. The modulation of nocturnal rainfall by upwelling intensity is not significant in 2016, may because $UI_{\Delta SST}$ is smaller than the cases of 2005 and 2010.

The variability in upwelling intensity is closely related with the pattern of atmospheric circulation in the decaying summer of El Niño years, but

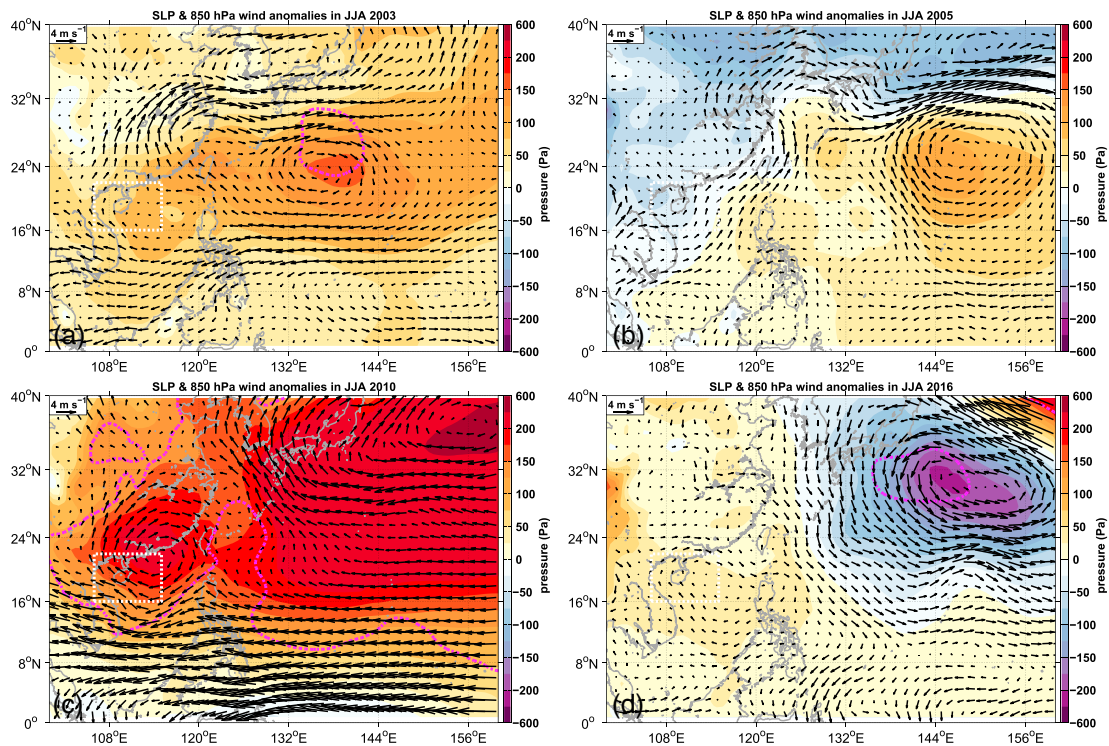


Figure 11. Sea level pressure (SLP) anomalies (Pa, color shading) and 850-hPa wind anomalies (vectors, m/s) in the decaying summer (June–August [JJA]) of El Niño events in (a) 2002/2003, (b) 2004/2005, (c) 2009/2010, and (d) 2015/2016. Anomalies are calculated as the monthly mean minus the multiyear summer average from 2000 to 2017. The magenta contours indicate where the value of anomalies exceeds the 95% significance level (t test).

different origins and patterns of SST anomalies (Wang & Wang, 2013). Accordingly, the 2002/2003 El Niño is classified as CP El Niño I, while 2004/2005 and 2009/2010 are classified as CP El Niño II, and 2015/2016 is the traditional EP El Niño. In the decaying summers of these four El Niño events, the atmospheric circulation in the western Pacific and SCS shows different patterns (Figure 11). For CP El Niño I, an oblate anticyclone resides over the NSCS and the Philippine Sea. This anomalous anticyclone produced southerly or southeasterly wind anomalies in 2003 and thus inhibited upwelling (Figure 11a). For CP El Niño II, the anomalous anticyclone shifted to the east of the Philippines (Figure 11b), leading to southwesterly wind anomalies that maintained normal upwelling at Hainan in 2005. In 2010, two strong anticyclones are identified in the NSCS and east of Japan (Figure 11c). The anomalous anticyclone over the NSCS produced strong southeasterly wind anomalies that suppressed the development of coastal upwelling. In the traditional EP El Niño, although an anomalous cyclone appears southeast of Japan, there are southeasterly wind anomalies at south Hainan that weaken the upwelling intensity (Figure 11d). Thus, there is a decrease in upwelling intensity when southeasterly wind anomalies occurs near southern Hainan, which could potentially change the diurnal cycle of rainfall at this area.

6. Numerical Simulations of the Modulation of Offshore Rainfall by Upwelling

6.1. Results of Control Run

The influence of upwelling on the island's rainfall is examined further through numerical simulations. Control runs using realistic SSTs and initial and boundary conditions were carried out in August 2010 and 2011. The simulated winds are first validated against the observations at the 11 AWS stations (Figure 1b) close to the southern coastline of Hainan. Sea and land breezes are clearly shown on the multi-year mean wind hodograph for August at these AWSs. Therefore, it is appropriate to validate the simulated sea and land breezes against the observations (Figure 12). In general, the WRF simulations overestimate the mean wind speed by 0.8–1.2 m/s and mean wind direction by 11–26° (Table 2). The observations show a northwesterly land breeze (WNW-NNW) and southwesterly sea breeze (SW-WSW) in 2010. The positive

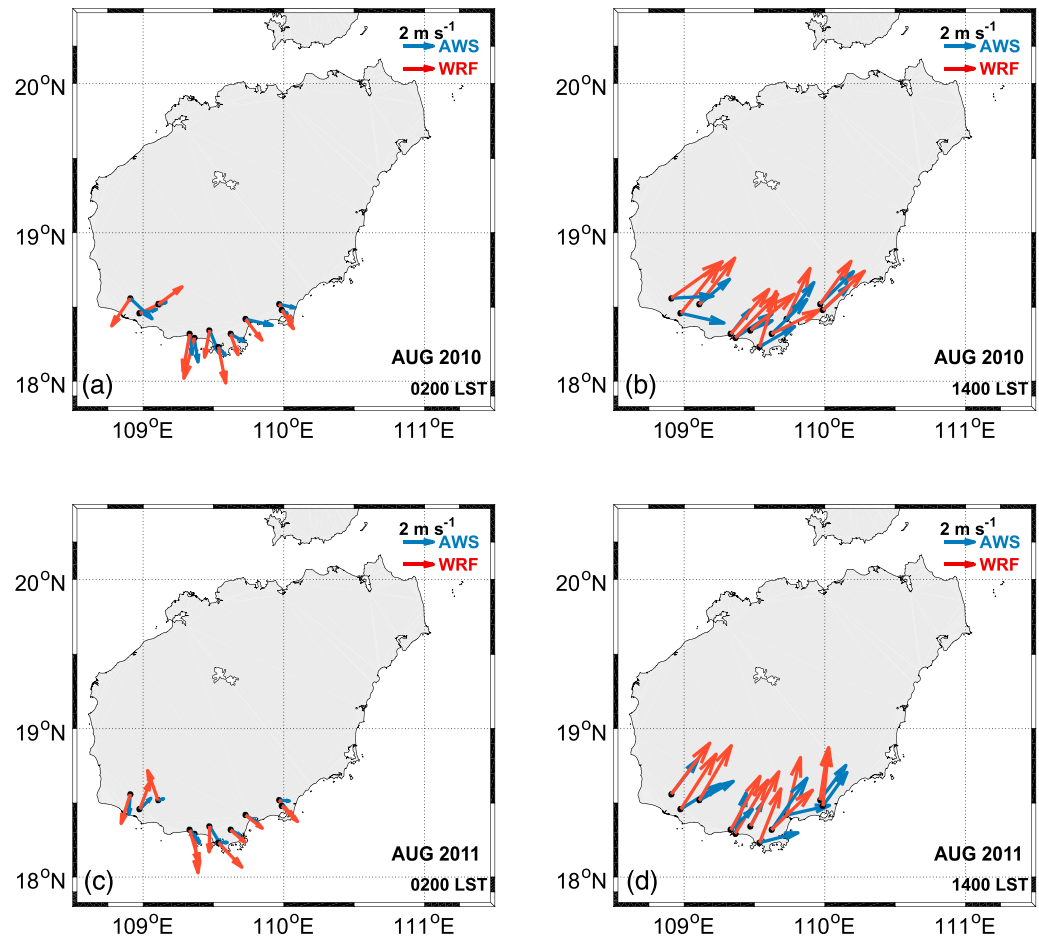


Figure 12. (a) Monthly mean winds (m/s) from automatic weather stations (AWSs; blue arrows) and the Weather Research and Forecasting (WRF) simulations (red arrows) at 0200 LST and 1400 LST (b) in August 2010, and the same in August 2011 (c, d).

differences in the wind directions at 0200 LST indicate that the simulated land breeze is blowing more southward (offshore, Figure 12a), and the negative differences at 1400 LST indicate that the simulated sea breeze is blowing more northward (onshore, Figure 12b). In addition, the observations show a stronger land breeze but weaker sea breeze in 2010 than in 2011 (Table 2). The WRF simulations produce the same change in the magnitudes of sea and land breezes in 2010 and 2011. Therefore, the WRF simulation could capture the major features of the sea and land breezes over southern Hainan and may be used for the further analysis of the modulation of coastal rainfall by the sea and land breezes.

The simulated rainfall is validated against 3B42RT data. The WRF simulation in August 2010 shows a similar spatial pattern of monthly mean rainfall to that derived from the 3B42RT dataset (Figure 13a). Heavy rainfall over Hainan and its surrounding area is simulated by the WRF model. The rainfall band over the southern and southeastern coastal sea is identifiable in the WRF simulation. However, compared with the merged satellite observations, the WRF simulation shows much stronger rainfall, over both land and sea. The intensity of rainfall in the WRF simulation is generally about 0.2–0.4 mm/hr higher than that in the 3B42RT data over the sea. There also seems to be a southward shift in the center of rainfall over land in the WRF simulation.

The WRF simulation gives a significant weakening in rainfall intensity over the sea in August 2011 (Figure 13b). The rainfall rate falls down from more than 0.8 mm/hr in 2010 to about 0.4 mm/hr in 2011 over the sea. The rainfall over land is also weakened in most areas, except in the southwest of the island (Figures 13b and 13c). Although the WRF simulations produce stronger rainfall than observed, the

Table 2
Validation of Simulated Sea and Land Breezes in the Control Runs for 2010 and 2011

| AWS no. | 02 LST Aug. 2010 | | | | 02 LST Aug. 2011 | | | |
|---------|------------------|--------------------|-----------|---------------------|------------------|--------------------|-----------|---------------------|
| | W_0 (m/s) | W_{0_dif} (m/s) | W_{dir} | W_{dir_diff} (°) | W_0 (m/s) | W_{0_dif} (m/s) | W_{dir} | W_{dir_diff} (°) |
| M01 | 1.65 | 1.17 | NNW | 23.29 | 0.73 | 1.92 | NW | 21.25 |
| M02 | 1.85 | -0.05 | WNW | 39.12 | 0.94 | 0.5 | WNW | 7.08 |
| M03 | 1.67 | 0.18 | NNW | 32.62 | 1.56 | 0.19 | NW | 31.52 |
| M04 | 0.74 | 1.75 | NW | 27.81 | 0.59 | 1.7 | W | 48.06 |
| M05 | 1.01 | 0.48 | NW | 40.92 | 0.71 | 0.56 | WNW | 12.87 |
| M06 | 1.37 | 1.18 | NNW | 17 | 1.04 | 1.34 | NW | 23.53 |
| M07 | 1.1 | 0.39 | WNW | 40.46 | 0.7 | 0.83 | W | 44.32 |
| M08 | 0.43 | 1.05 | NNW | 25.92 | 0.15 | 1.34 | WNW | 37.27 |
| M09 | 1.16 | 0.8 | WSW | -12.42 | 1.04 | 0.94 | SW | -24.69 |
| M10 | 0.55 | 1.46 | WSW | -21.7 | 0.39 | 1.75 | WSW | -92.28 |
| M11 | 2.02 | 0.23 | NW | 80.67 | 1.37 | 0.7 | NNW | 13.4 |
| Average | 1.23 | 0.78 | — | 26.70 | 0.83 | 1.07 | — | 11.12 |

| AWS no. | 14 LST Aug. 2010 | | | | 14 LST Aug. 2011 | | | |
|---------|------------------|--------------------|-----------|---------------------|------------------|--------------------|-----------|---------------------|
| | W_0 (m/s) | W_{0_dif} (m/s) | W_{dir} | W_{dir_diff} (°) | W_0 (m/s) | W_{0_dif} (m/s) | W_{dir} | W_{dir_diff} (°) |
| M01 | 2.97 | 1.14 | WSW | -12.67 | 2.85 | 1.38 | SSW | 16.41 |
| M02 | 3.09 | 0.68 | SW | -11.99 | 2.98 | 1.02 | WSW | -63.63 |
| M03 | 1.59 | 2.23 | WSW | -15.57 | 1.69 | 2.44 | SSW | 0.49 |
| M04 | 2.75 | 1.16 | WSW | -43.2 | 2.68 | 1.23 | WSW | -53.76 |
| M05 | 3.34 | 0.3 | SW | 17.67 | 4.23 | -0.38 | SSW | 11.39 |
| M06 | 2.07 | 1.89 | WSW | 2.22 | 2.02 | 2.11 | SW | -17.85 |
| M07 | 3.15 | 0.42 | SW | -9.84 | 2.92 | 0.53 | SSW | -28.01 |
| M08 | 2.39 | 1.44 | SW | -0.09 | 2.78 | 1.17 | SSW | -30.04 |
| M09 | 2.99 | 1.34 | WNW | -64.08 | 3.17 | 1.24 | WSW | -25.05 |
| M10 | 2.67 | 1.28 | WSW | -12.73 | 2.64 | 1.64 | WSW | -30.32 |
| M11 | 2.82 | 1.42 | WSW | -32.65 | 2.97 | 1.34 | SSW | -0.47 |
| Average | 2.71 | 1.20 | — | -16.63 | 2.82 | 1.24 | — | -20.07 |

Note. WRF simulations are validated by the observations of 11 AWSs close to the southern coastline of Hainan (Figure 1b). W_0 and W_{dir} denote the observed monthly mean wind speed and meteorological wind direction, respectively. W_{0_dif} and W_{dir_diff} are the differences between the simulation results and observations (i.e., WRF minus observation). The simulated wind speed and directions are validated at 0200 LST and 1400 LST to examine the strength of land and sea breezes, respectively. AWS = automatic weather station; WRF = Weather Research and Forecasting.

differences in rainfall intensity and spatial pattern between August 2010 and 2011 are mostly captured by the WRF simulations. The variation in the diurnal cycle of rainfall is also simulated by the WRF model. The diurnal cycle in the control runs not only shows an apparent enhancement in the nocturnal offshore rainfall southeast of Hainan in 2010 (Figure 14) but also a stronger increase in offshore rainfall in the afternoon than seen in the TRMM data. This means that the increase in rainfall off southern Hainan shown in Figure 13c may be overestimated. Note that the diurnal cycle of the WRF simulation shows a southeastward shift in the offshore rainfall band from 0500 to 0800 LST (Figure 14), which seems to be a gravity-wave propagation process associated with the mesoscale convective systems that occurred in 2010; this will be studied further in future work.

6.2. Sensitivity Experiments

Since the control runs simulate the major feature of the variation in rainfall around Hainan in August 2010 and 2011, three additional experiments are carried out to examine the influence of upwelling on the rainfall over Hainan, especially its diurnal cycle. The first experiment uses the SST in August 2011 (normal upwelling) to carry out the simulation for August 2010 (hereafter the 2010S run). The second experiment uses the SST in August 2010 (weak upwelling) to carry out the simulation for August 2011 (2011S run), and the third is also run for 2011 but with the SST being 1 K higher than in the 2011S run (2011SP1 run). In the sensitivity experiments, only the SST in the inner domain is changed; the other model parameters, as well as the initial and boundary conditions, remain the same as in the control run.

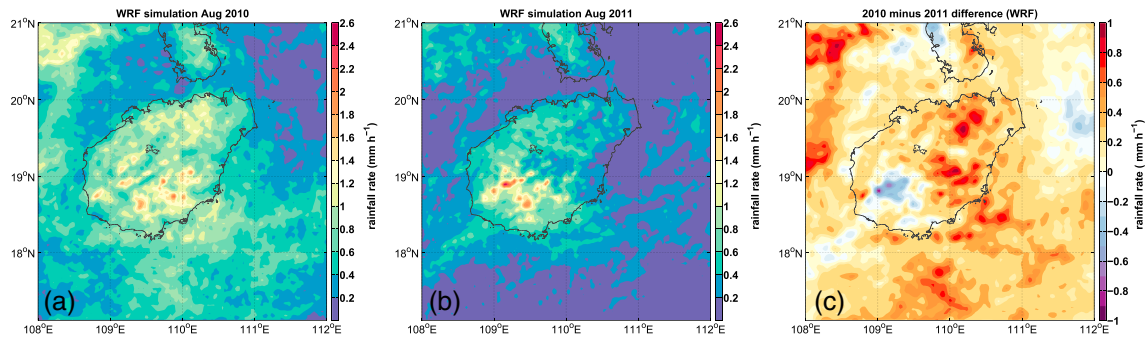


Figure 13. (a) Monthly mean rainfall rate (mm/hr) from the control run of the Weather Research and Forecasting (WRF) simulation in August 2010. (b) The same as (a) but in August 2011. (c) The difference between 2010 and 2011 (i.e., 2010 minus 2011).

The 2011S results are discussed first because the influence of upwelling intensity on the monthly mean rainfall can be identified very clearly in this case (Figure 15a). Compared with the control run in August 2011 (Figure 13b), the warm coastal SST due to weak upwelling leads to an apparent increase in the rainfall off the southern coast (Figure 15b). The intensity of rainfall over land is generally reduced, except over some areas in the north of the island (Figure 15b). The response of the diurnal cycle of rainfall to the weak upwelling is also simulated well in 2011S. Nocturnal rainfall intensity is significantly enhanced off the southern coast from 0200 LST to 0800 LST, while the change in offshore rainfall intensity at other times is not significantly larger than the background value over the sea (0.2 mm/hr, Figure 16). The southern offshore rainfall is weakened at 1100 LST and the rainfall over land in the north of the island is weakened at 1700 LST. The variation in offshore rainfall and rainfall over land in 2011S suggests that the variation in upwelling intensity could influence the diurnal cycle of rainfall at south Hainan, and this process may be closely related to the sea and land breeze circulation.

The modulation of the land breeze by the upwelling is further investigated in the 2011S case. The results of the control run show that the surface wind is generally northward over the sea in the middle of the night (black vectors in Figures 17a and 17b). The surface wind turns to blow along the coastline as it approaches the nearshore area off the island because of the effect of the land breeze. The land breeze does not reverse the direction of the onshore wind but rotates the nearshore wind direction clockwise off the southeastern coast and anticlockwise off the southwestern coast (red vectors in Figures 17a and 17b). The sensitivity run 2011S

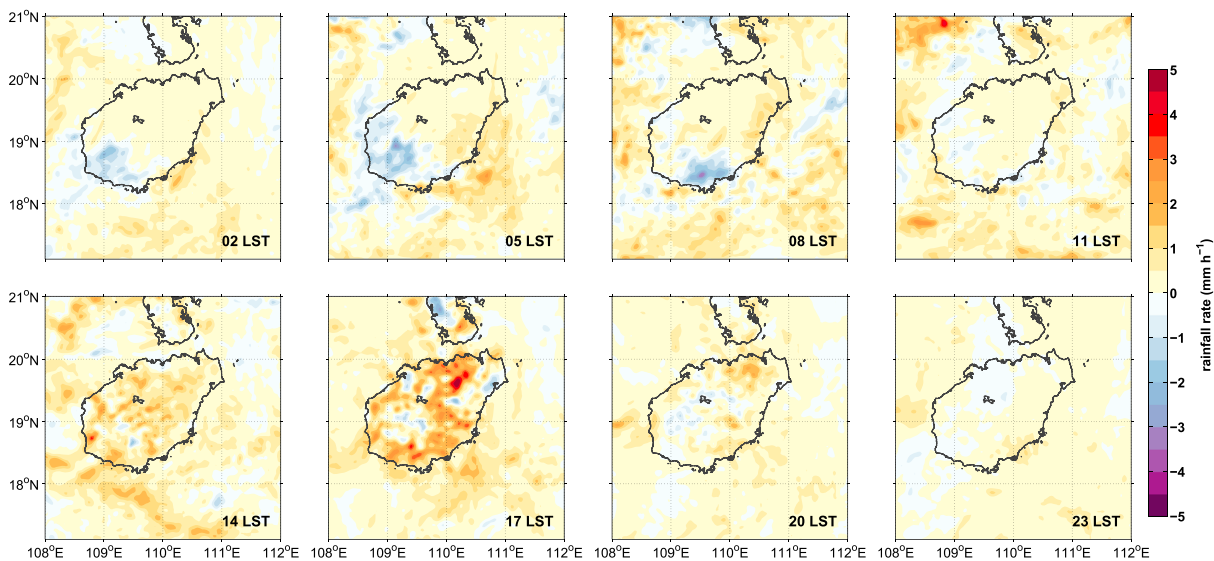


Figure 14. Diurnal cycle of rainfall rate difference (mm/hr) between the control runs of August 2010 and 2011 (i.e., 2010 minus 2011).

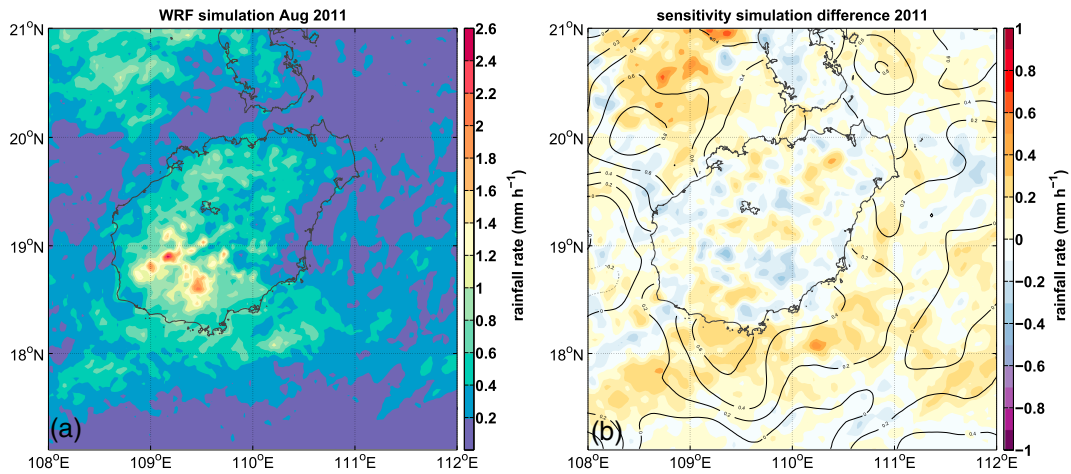


Figure 15. (a) Monthly mean rainfall rate (mm/hr) from the sensitivity simulation of 2011 with 2010 SST (2011S). (b) The difference between the sensitivity simulation and the control run results. Contour lines in (b) denote the sea surface temperature difference in the sensitivity simulations from the values in the control run. WRF = Weather Research and Forecasting.

simulates a much stronger land breeze (red vectors in Figures 17c and 17d) due to the increase in SST_{coast} associated with weak upwelling. The wind is blowing offshore and almost perpendicular to the coastline as it approaches the southern coastal sea. The land breeze gradually strengthens from the coastline and reaches its maximum magnitude over the sea a few kilometers away (Figure 17e and 17f), where the enhanced land breeze—due to weak upwelling—produces stronger convergence at the surface that may eventually lead to a synchronous intensification of rainfall shown in Figure 16.

The warm SST_{coast} due to weak upwelling enhances the land-ocean thermal contrast at night but reduces it during the daytime. As a result, the land breeze is intensified but the sea breeze is weakened on the land. The simulated surface winds in the 2011 control run generally blow northeastward over the sea in the afternoon, and a landward rotation in wind direction occurs near the coastline of the island due to the onshore sea breeze (black vectors in Figures 18a and 18b). It can be seen that the landward rotation of the prevailing wind is weakened in the 2011S case (red vectors in Figures 18a and 18b). Warm SST_{coast} in the 2011S case

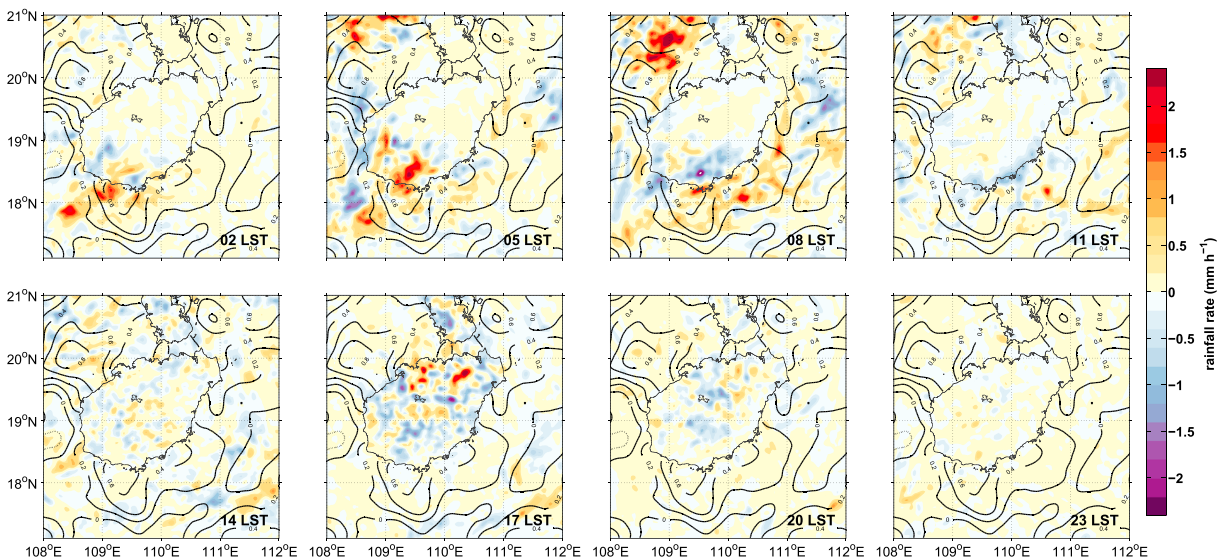


Figure 16. Diurnal cycle of rainfall rate difference (mm/hr) calculated for the sensitivity experiment minus the control run for August 2011. Black contours indicate the sea surface temperature difference between the sensitivity and control runs; solid contours indicate an increase in sea surface temperature and weakening of upwelling in the sensitivity experiment.

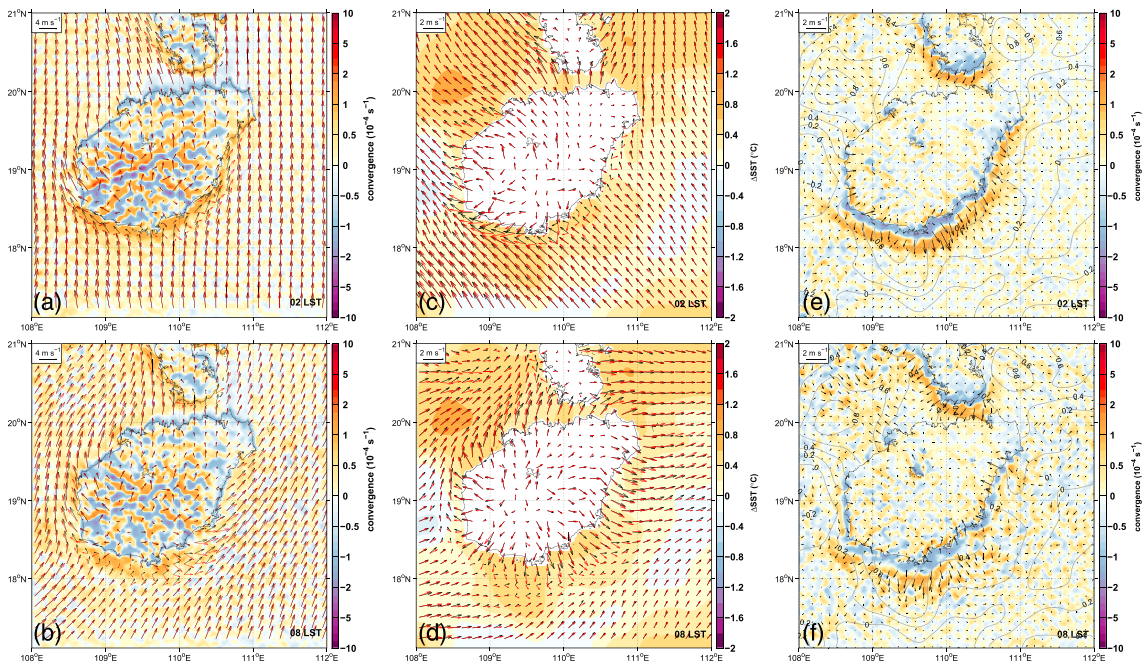


Figure 17. (a, b) Monthly mean surface wind (m/s, vectors) and convergence field (s^{-1} , color shading) from the Weather Research and Forecasting simulations of the control run and sensitivity run for August 2011 at 0200 LST and 0800 LST. (c, d) Monthly mean land breeze (m/s, calculated by removing the daily mean from the hourly wind). (e, f) The difference of land breeze and convergence (i.e., sensitivity run minus control run). The black vectors in (a–d) are the results of the control run and the red vectors denote the sensitivity run with weak upwelling in 2011 (2011S). SST = sea surface temperature.

reduces the land-ocean thermal contrast nearshore, so the sea breeze is weakened in the area near the coastline (Figures 18c and 18d). The weakened sea breeze reduces the strength of surface wind convergence in the inland area (Figures 18e and 18f), which leads to a reduction in rainfall over land during the afternoon (Figure 16). There is an increase in the sea breeze over the sea away from the coastline in the 2011S case.

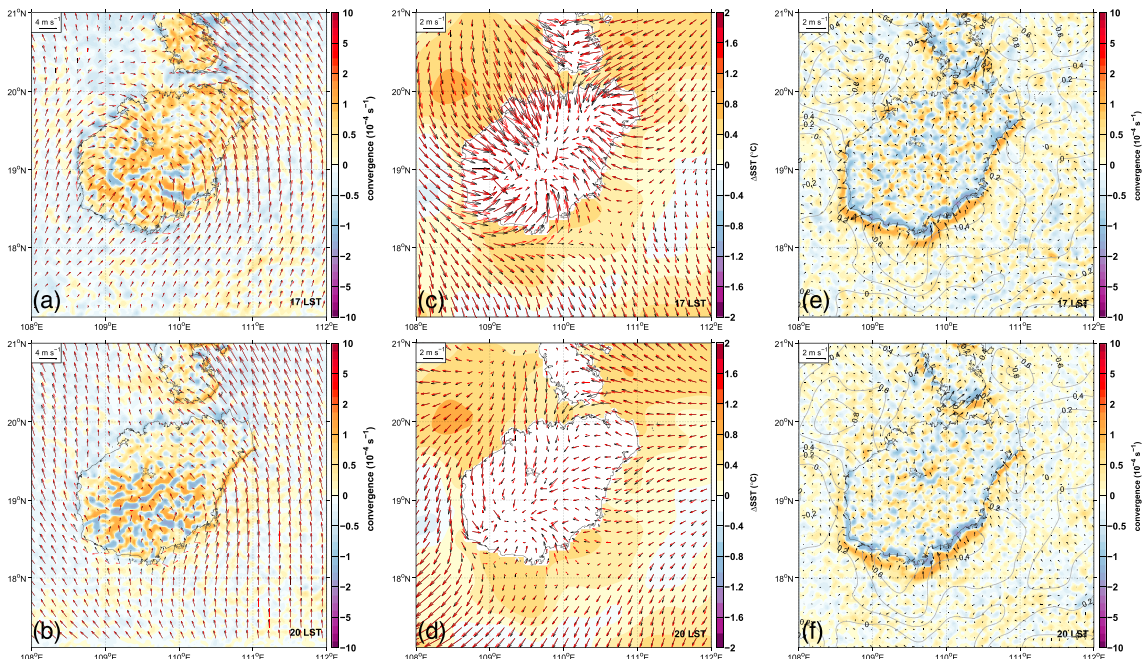


Figure 18. As in Figure 17 but for 1700 LST and 2000 LST. WRF = Weather Research and Forecasting.

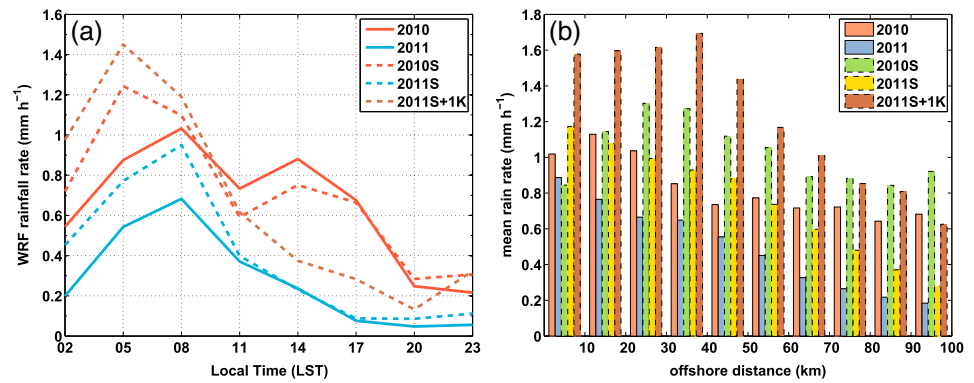


Figure 19. (a) Diurnal cycle of the spatially averaged rainfall rate in the coastal region delineated by the dashed line in Figure 9a. (b) Spatially binned nocturnal (0200–0800 LST) rainfall rate versus the distance from the southern coastline of Hainan. Red solid (dashed) lines in (a) denote the results of the control (sensitivity) run for 2010, while the blue lines show the results for 2011. The brown dashed line represents the results of the sensitivity experiment 2011SP for 2011 that uses the sea surface temperature of August 2010 increased by 1 K. Colors in (b) refer to the same control and sensitivity simulations.

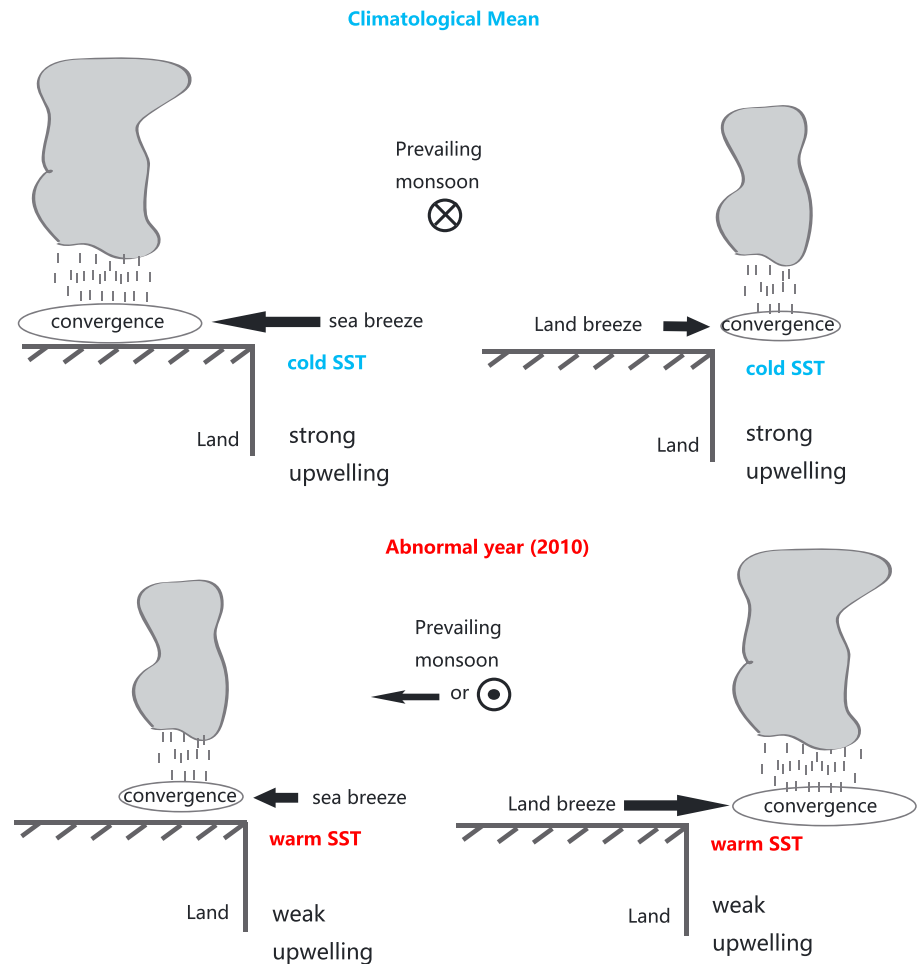


Figure 20. Schematic summary of this study. SST = sea surface temperature.

It is caused by the modulation of local SST on the hourly wind and daily mean wind both and has little influence on the convergence on the land.

The sensitivity experiment with normal upwelling in 2010 (2010S) simulates stronger nocturnal rainfall than the control run over the coastal region of south Hainan (Figure 19a). This seems to contradict the previous result. However, there is a significant difference in the maximum rainfall area simulated by the control and 2010S runs. The maximum rainfall simulated by the control run of 2010 occurs in the region from 10 to 20 km offshore (orange bars in Figure 19b). In contrast, the 2010S run simulates maximum rainfall in the region that is nearly 30 km from the coastline (green bars in Figure 19b). Therefore, the rainfall processes in these two cases may be different. The main reason for the “intensified rainfall” in the 2010S case is the adjustment of the wind field to the artificial upwelling. In the 2010S case, the southeasterly sea surface wind still blows onshore from warm water to cold water across the upwelling zone. The wind speed is reduced at the cold side of the SST front associated with upwelling (figures not shown) because of the positive SST-wind coupling process mentioned in the introduction part. Thus, there is a convergence zone that is suppressed by enhanced vertical motion and rainfall over the frontal area (Chelton et al., 2004; Minobe et al., 2008; Small et al., 2008; Toy & Johnson, 2014), and this process may confound the effects of the land breeze in the 2010S run.

The 2011SP1 run simulates the most intense rainfall of the five simulations (Figure 19a). Note that the intensification of rainfall is much stronger in the nighttime than the daytime. The nocturnal rainfall rate in 2011SP1 is almost double that in 2011S whereas the daytime rainfall rate is only slightly different (Figure 19a). This asymmetric intensification of rainfall further illustrates the importance of the land breeze in modulating the nocturnal rainfall. In addition, the positive effect of warming SST on rainfall decays with distance offshore. The most evident enhancement of rainfall simulated in 2011SP1 is restricted to an area within 70 km of the coastline. At offshore distances greater than 70 km, the rainfall in the 2011SP1 case is comparable to that in the control run for 2010 (Figure 19b). This shows that the influence of the local SST change is limited, although it may significantly change the surface moisture flux and coastal rainfall. The change in local SST can regulate the diurnal cycle of rainfall over an island according to its influence on mesoscale processes such as sea or land breezes, but it does not have a similar impact on the regional climate as the midlatitude SST front does (Kuwano-Yoshida & Minobe, 2017; Small et al., 2014).

7. Discussion and Conclusions

The modulation of coastal rainfall at Hainan, South China, by the large-scale circulation and coastal upwelling has been studied using observations and numerical simulations. Both radar observations and the TRMM 3B42RT data show a pronounced difference in the monthly mean rainfall off the southern coast of Hainan between August 2010 and 2011, with much greater rainfall in the former case than the latter. With respect to an 18-year average of TRMM 3B42RT data, there are significant positive anomalies in offshore rainfall during August 2010 but negative anomalies in 2011. Furthermore, the main contributor to the anomalously high offshore rainfall in August 2010 is the intensification of rainfall at night.

ERA-Interim and radiosonde data have been used to investigate the relationship between the atmospheric circulation and the change of rainfall intensity in August 2010 and 2011. Compared with the multiyear (2000–2017) average field, there is an apparent increase in the water vapor concentration from the surface to 500 hPa in 2010. There were easterly monsoon anomalies over the SCS and western equatorial Pacific in August 2010, and these anomalies were much stronger in 2010 than in other years when a decaying El Niño was confirmed. The anomalous atmospheric circulation leads to wet anomalies over the SCS in 2010 and produces a general intensification of total rainfall over Hainan and its surrounding area. This result differs from previous findings that there are dry anomalies over the SCS in the decaying summer of El Niño events because of the anomalous anticyclone over the western Pacific (Tao et al., 2016).

The analysis of convective instability shows that the variation in large-scale circulation results in little change in the CAPE during August 2010 and 2011 at Hainan. However, the change in atmospheric circulation does modulate the coastal upwelling system at Hainan. An upwelling index $UI_{\Delta SST}$ is defined to quantify the annual variation of upwelling intensity since 2000. Decreases in upwelling intensity were confirmed in the decaying summers of the 2002/2003, 2009/2010, and 2015/2016 El Niño but not in the 2004/2005 El Niño. The anomalous onshore-blowing wind associated with southeasterly wind anomalies depresses

the development of upwelling and a warm SST appears off southern Hainan. Meanwhile, the warm SST near the coast increases the land-sea thermal contrast and changes the strength of the sea and land breezes, which results in an increasing in nocturnal offshore rainfall but little change in daytime offshore rainfall in the summers of 2003 and 2010. The increase in nocturnal rainfall during the other two El Niño events is not significant, possibly because upwelling intensity is not apparently weakened.

The modulation of the surface wind convergence by the upwelling may be the major reason for the variation in the diurnal cycle of rainfall, and this modulation has been examined using numerical simulations. The sensitivity experiment of the WRF simulation for August 2011 shows that the warm sea surface due to weak upwelling produces a stronger land breeze and surface convergence over the sea, ultimately leading to an intensification of rainfall off the southern coast of Hainan at night (Figure 20d). Weak upwelling also reduced the strength and extent of the sea breeze, causing weak convergence and less inland rainfall (Figure 20c). In contrast, well-developed upwelling suppressed (enhanced) the land (sea) breeze, producing less offshore rainfall but more inland rainfall for a normal year (Figures 20a and 20b). Although direct convection forcing by warm SST anomalies could increase rainfall intensity, the surface convergence induced by sea or land breeze is a more important process to be considered, especially for the nocturnal rain off the coastline of a tropical island.

Therefore, our final conclusion is that the anomalous atmospheric circulation in the decaying summer of El Niño events is usually unfavorable for the developing of upwelling off southern Hainan. As a result, the diurnal cycle of rainfall, which is significantly regulated by the upwelling intensity, is also changed around Hainan. It is also noticed that there are still some uncertainties due to the complexity of El Niño itself and the processes in the coastal sea (Li et al., 2018; Su et al., 2013), which needs more studies in the future.

Acknowledgments

All data used in this study are available at <https://pmm.nasa.gov/data-access/downloads/trmm> for TRMM precipitation, <https://apps.ecmwf.int/datasets/data/interim-full-daily/levtype=sfc/> for ERA-Interim reanalysis data, http://ghrsst-pp.metoffice.com/pages/latest_analysis/ostia.html for OSTIA SST, http://apdrc.soest.hawaii.edu/data/data.php?discipline_index=3 for QuikSCAT & ASCAT wind, <https://rda.ucar.edu/datasets/ds083.2/index.html#description> for soil temperature and moisture data, and <https://doi.org/10.6084/m9.figshare.7447166.v4> for radiosonde and numerical simulation results. This research was supported by the Frontier Science Research Project of Chinese Academy of Sciences (Grant QYZDJ-SSW-DQC022), the National Natural Science Foundation of China (Grants 41676018, 41476014, and 41576002), the Science and Technology Planning Project of Guangdong Province, China (2016A020224003), and the Ministry of Education, Culture, Sports, Science and Technology, Japan (MEXT) to a project on Joint Usage/Research Center-Leading Academia in Marine and Environment Pollution Research (LaMer). The numerical simulation was run with the support of the High-Performance Computing Division of the South China Sea Institute of Oceanology and Ms. Dandan Sui.

References

- Ashok, K., Behera, S. K., Rao, S. A., Weng, H., & Yamagata, T. (2007). El Niño Modoki and its possible teleconnection. *Journal of Geophysical Research*, *112*, C11007. <https://doi.org/10.1029/2006JC003798>
- Birch, C. E., Webster, S., Peatman, S. C., Parker, D. J., Matthews, A. J., Li, Y., & Hassim, M. E. E. (2016). Scale interactions between the MJO and the western maritime continent. *Journal of Climate*, *29*(7), 2471–2492. <https://doi.org/10.1175/JCLI-D-15-0557.1>
- Boé, J., Hall, A., Colas, F., McWilliams, J. C., Qu, X., Kurian, J., & Kapnick, S. B. (2011). What shapes mesoscale wind anomalies in coastal upwelling zones? *Climate Dynamics*, *36*(11–12), 2037–2049. <https://doi.org/10.1007/s00382-011-1058-5>
- Bolton, D. (1980). The computation of equivalent potential temperature. *Monthly Weather Review*, *108*(7), 1046–1053. [https://doi.org/10.1175/1520-0493\(1980\)108<1046:TCOEPT>2.0.CO;2](https://doi.org/10.1175/1520-0493(1980)108<1046:TCOEPT>2.0.CO;2)
- Chelton, D. B. (2013). Ocean-atmosphere coupling: Mesoscale eddy effects. *Nature Geoscience*, *6*(8), 594–595. <https://doi.org/10.1038/ngeo1906>
- Chelton, D. B., Schlax, M. G., Freilich, M. H., & Milliff, M. H. (2004). Satellite measurements reveal persistent small-scale features in ocean winds. *Science*, *303*(5660), 978–983. <https://doi.org/10.1126/science.1091901>
- Chen, F., & Dudhia, J. (2001). Coupling an advanced land surface hydrology model with the penn state ncar mm5 modeling system. Part I: Model implementation and sensitivity. *Monthly Weather Review*, *129*(4), 569–585. [https://doi.org/10.1175/1520-0493\(2001\)129<0569:CAALSH>2.0.CO;2](https://doi.org/10.1175/1520-0493(2001)129<0569:CAALSH>2.0.CO;2)
- Chen, G., Sha, W., Sawada, M., & Iwasaki, T. (2013). Influence of summer monsoon diurnal cycle on moisture transport and precipitation over eastern China. *Journal of Geophysical Research: Atmospheres*, *118*, 3163–3177. <https://doi.org/10.1002/jgrd.50337>
- Chow, C. H., & Liu, Q. (2012). Eddy effects on sea surface temperature and sea surface wind in the continental slope region of the northern South China Sea. *Geophysical Research Letters*, *39*, L02601. <https://doi.org/10.1029/2011GL050230>
- Chu, P. C., & Wang, G. H. (2003). Seasonal variability of thermohaline front in the central South China Sea. *Journal of Oceanography*, *59*(1), 65–78. <https://doi.org/10.1023/A:1022868407012>
- Czaja, A., & Blunt, N. (2011). A new mechanism for ocean–atmosphere coupling in midlatitudes. *Quarterly Journal of the Royal Meteorological Society*, *137*(657), 1095–1101. <https://doi.org/10.1002/qj.814>
- Dee, D. P., Uppala, S. M., Simmons, A. J., Berrisford, P., Poli, P., Kobayashi, S., et al. (2011). The era-interim reanalysis: Configuration and performance of the data assimilation system. *Quarterly Journal of the Royal Meteorological Society*, *137*(656), 553–597. <https://doi.org/10.1002/qj.828>
- Donlon, C. J., Martin, M., Stark, J., Roberts-Jones, J., Fiedler, E., & Wimmer, W. (2012). The Operational sea surface temperature and sea ice analysis (OSTIA) system. *Remote Sensing of Environment*, *116*(2), 140–158. <https://doi.org/10.1016/j.rse.2010.10.017>
- Du, Y., Xie, S., Huang, G., & Hu, K. (2009). Role of air–sea interaction in the long persistence of El Niño–induced North Indian Ocean warming. *Journal of Climate*, *22*(8), 2023–2038. <https://doi.org/10.1175/2008JCLI2590.1>
- Dudhia, J. (1989). Numerical study of convection observed during the winter monsoon experiment using a mesoscale two-dimensional model. *Journal of the Atmospheric Sciences*, *46*(20), 3077–3107. [https://doi.org/10.1175/1520-0469\(1989\)046<3077:NSOCOD>2.0.CO;2](https://doi.org/10.1175/1520-0469(1989)046<3077:NSOCOD>2.0.CO;2)
- Gan, J. P., Li, L., Wang, D. X., & Guo, X. G. (2009). Interaction of a river plume with coastal upwelling in the northeastern South China Sea. *Continental Shelf Research*, *29*(4), 728–740. <https://doi.org/10.1016/j.csr.2008.12.002>
- Hong, S. Y., & Lim, J. O. J. (2006). The WRF Single-Moment 6-class Microphysics Scheme (WSM6). *Journal of the Korean Meteorological Society*, *42*, 129–151.
- Houze, R. A. J., Geotis, S. G., Marks, F. D. Jr., & West, A. K. (1981). Winter monsoon convection in the vicinity of North Borneo. Part I: Structure and time variation of the clouds and precipitation. *Monthly Weather Review*, *109*(8), 1595–1614. [https://doi.org/10.1175/1520-0493\(1981\)109<1595:WMCITV>2.0.CO;2](https://doi.org/10.1175/1520-0493(1981)109<1595:WMCITV>2.0.CO;2)

- Hu, J. Y., Kawamura, H., Hong, H. S., Suetsugu, M., & Lin, M. S. (2001). Hydrographic and satellite observations of summertime upwelling in the Taiwan Strait: A preliminary description. *Terrestrial, Atmospheric and Oceanic Sciences*, *12*(2), 415–430. [https://doi.org/10.3319/TAO.2001.12.2.415\(O\)](https://doi.org/10.3319/TAO.2001.12.2.415(O))
- Hu, J. Y., Kawamura, H., & Tang, D.-L. (2003). Tidal front around the Hainan Island, northwest of the South China Sea. *Journal of Geophysical Research*, *108*(C11), 3342. <https://doi.org/10.1029/2003JC001883>
- Hu, K., Xie, S.-P., Huang, G., Hu, K., Xie, S. P., & Huang, G. (2017). Orographically anchored El Niño effect on summer rainfall in Central China. *Journal of Climate*, *30*(24), 10,037–10,045. <https://doi.org/10.1175/JCLI-D-17-0312.1>
- Huang, R. H., Zhang, R.-H., & Zhang, Q.-Y. (2000). The 1997/98 ENSO cycle and its impact on summer climate anomalies in East Asia. *Advances in Atmospheric Sciences*, *17*(3), 348–362. <https://doi.org/10.1007/s00376-000-0028-3>
- Ichikawa, H., & Yasunari, T. (2006). Time–space characteristics of diurnal rainfall over Borneo and surrounding oceans as observed by TRMM-PR. *Journal of Climate*, *19*(7), 1238–1260. <https://doi.org/10.1175/JCLI3714.1>
- Jing, Z., Qi, Y., Du, Y., Zhang, S., & Xie, L. (2015). Summer upwelling and thermal fronts in the northwestern South China Sea: Observational analysis of two mesoscale mapping surveys. *Journal of Geophysical Research: Oceans*, *120*, 1993–2006. <https://doi.org/10.1002/2014JC010601>
- Johnson, R. H., & Priegnitz, D. L. (1981). Winter monsoon convection in the vicinity of North Borneo. Part II: Effects on large-scale fields. *Monthly Weather Review*, *109*(8), 1615–1628. [https://doi.org/10.1175/1520-0493\(1981\)109<1615:WMCITV>2.0.CO;2](https://doi.org/10.1175/1520-0493(1981)109<1615:WMCITV>2.0.CO;2)
- Kamimera, H., Mori, S., Yamanaka, M. D., & Syamsudin, F. (2012). Modulation of diurnal rainfall cycle by the Madden-Julian oscillation based on one-year continuous observations with a meteorological radar in West Sumatra. *Scientific Online Letters on the Atmosphere: Sola*, *5*(1), 111–114. <https://doi.org/10.1186/s40645-018-0202-9>
- Kanamori, H., Yasunari, T., & Kuraji, K. (2013). Modulation of the diurnal cycle of rainfall associated with the MJO observed by a dense hourly rain gauge network at Sarawak, Borneo. *Journal of Climate*, *26*(13), 4858–4875. <https://doi.org/10.1175/JCLI-D-12-00158.1>
- Keenan, T. D., & Carbone, R. E. (2007). Propagation and diurnal evolution of warm season cloudiness in the Australian and maritime continent region. *Monthly Weather Review*, *136*(3), 973–994. <https://doi.org/10.1175/2007MWR2152.1>
- Kikuchi, K., & Wang, B. (2008). Diurnal precipitation regimes in the global tropics. *Journal of Climate*, *21*(11), 2680–2696. <https://doi.org/10.1175/2007JCLI2051.1>
- Kilpatrick, T., & Xie, S.-P. (2015). ASCAT observations of downdrafts from mesoscale convective systems. *Geophysical Research Letters*, *42*, 1951–1958. <https://doi.org/10.1002/2015GL063025>
- Kilpatrick, T., Xie, S.-P., & Nasuno, T. (2017). Diurnal convection-wind coupling in the Bay of Bengal. *Journal of Geophysical Research: Atmospheres*, *122*, 9705–9720. <https://doi.org/10.1002/2017JD027271>
- Koh, T. Y., & Teo, C. K. (2009). Toward a mesoscale observation network in Southeast Asia. *Bulletin of the American Meteorological Society*, *90*(4), 481–488. <https://doi.org/10.1175/2008BAMS2561.1>
- Kuwano-Yoshida, A., & Minobe, S. (2017). Storm-track response to SST fronts in the northwestern Pacific region in an AGCM. *Journal of Climate*, *30*(3), 1081–1102. <https://doi.org/10.1175/JCLI-D-16-0331.1>
- Li, Y., Peng, S., Wang, J., Yan, J., & Huang, H. (2018). On the mechanism of the generation and interannual variations of the summer upwellings west and southwest off the Hainan Island. *Journal of Geophysical Research: Oceans*, *123*, 8247–8263. <https://doi.org/10.1029/2018JC014226>
- Liu, Q.-Y., Wang, D., Wang, X., Shu, Y., Xie, Q., & Chen, J. (2014). Thermal variations in the South China Sea associated with the eastern and Central Pacific El Niño events and their mechanisms. *Journal of Geophysical Research: Oceans*, *119*, 8955–8972. <https://doi.org/10.1002/2014JC010429>
- Love, B. S., Matthews, A. J., & Lister, G. M. S. (2011). The diurnal cycle of precipitation over the Maritime Continent in a high-resolution atmospheric model. *Quarterly Journal of the Royal Meteorological Society*, *137*(657), 934–947. <https://doi.org/10.1002/qj.809>
- Mao, J. Y., & Wu, G. X. (2012). Diurnal variations of summer precipitation over the Asian monsoon region as revealed by TRMM satellite data. *Science China Earth Sciences*, *55*(4), 554–566. <https://doi.org/10.1007/s11430-011-4315-x>
- Mapes, B., Milliff, R., & Morzel, J. (2009). Composite life cycle of maritime tropical mesoscale convective systems in scatterometer and microwave satellite observations. *Journal of the Atmospheric Sciences*, *66*(1), 199–208. <https://doi.org/10.1175/2008JAS2746.1>
- Mapes, B. E., Warner, T. T., & Xu, M. (2003). Diurnal patterns of rainfall in northwestern South America. Part III: Diurnal gravity waves and nocturnal convection offshore. *Monthly Weather Review*, *131*(5), 830–844. [https://doi.org/10.1175/1520-0493\(2003\)131<0830:DPORIN>2.0.CO;2](https://doi.org/10.1175/1520-0493(2003)131<0830:DPORIN>2.0.CO;2)
- Miller, S. T. K., Keim, B. D., Talbot, R. W., & Mao, H. (2003). Sea breeze: Structure, forecasting, and impacts. *Reviews of Geophysics*, *41*(3), 1011. <https://doi.org/10.1029/2003RG000124>
- Minobe, S., Kuwanoyoshida, A., Komori, N., Xie, S. P., & Small, R. J. (2008). Influence of the Gulf Stream on the troposphere. *Nature*, *452*(7184), U206–U251.
- Mlawer, E. J., Taubman, S. J., Brown, P. D., Iacono, M. J., & Clough, S. A. (1997). Radiative transfer for inhomogeneous atmospheres: RRTM, a validated correlated-k model for the longwave. *Journal of Geophysical Research*, *102*(D14), 16,663–16,682. <https://doi.org/10.1029/97JD00237>
- Nakamura, H., Nishina, A., & Minobe, S. (2012). Response of storm tracks to bimodal Kuroshio path states south of Japan. *Journal of Climate*, *25*(21), 7772–7779. <https://doi.org/10.1175/JCLI-D-12-00326.1>
- Nakanishi, M., & Niino, H. (2006). An improved Mellor–Yamada level-3 model: Its numerical stability and application to a regional prediction of advection fog. *Boundary-Layer Meteorology*, *119*(2), 397–407. <https://doi.org/10.1007/s10546-005-9030-8>
- Nesbitt, S. W., & Zipser, E. J. (2003). The diurnal cycle of rainfall and convective intensity according to three years of TRMM measurements. *Journal of Climate*, *16*(10), 1456–1475. <https://doi.org/10.1175/1520-0442.16.10.1456>
- O'Neill, L. W., Esbensen, S. K., Thum, N., Samelson, R. M., & Chelton, D. B. (2010). Dynamical analysis of the boundary layer and surface wind responses to mesoscale SST perturbations. *Journal of Climate*, *23*(3), 559–581. <https://doi.org/10.1175/2009JCLI2662.1>
- Peatman, S. C., Matthews, A. J., & Stevens, D. P. (2014). Propagation of the Madden-Julian Oscillation through the Maritime Continent and scale interaction with the diurnal cycle of precipitation. *Quarterly Journal of the Royal Meteorological Society*, *140*(680), 814–825. <https://doi.org/10.1002/qj.2161>
- Perlin, N., Skillingstad, E. D., Samelson, R. M., & Barbour, P. L. (2007). Numerical simulation of air sea coupling during coastal upwelling. *Journal of Physical Oceanography*, *37*(8), 2081–2093. <https://doi.org/10.1175/JPO3104.1>
- Perlin, N., Szoek, S. P. D., Chelton, D. B., Samelson, R. M., Skillingstad, E. D., & O'Neill, L. W. (2014). Modeling the atmospheric boundary layer wind response to mesoscale sea surface temperature perturbations. *Monthly Weather Review*, *142*(11), 4284–4307. <https://doi.org/10.1175/MWR-D-13-00332.1>

- Sahany, S., Venugopal, V., & Nanjundiah, R. S. (2010). Diurnal-scale signatures of monsoon rainfall over the Indian region from TRMM satellite observations. *Journal of Geophysical Research*, *115*, D02103. <https://doi.org/10.1029/2009JD012644>
- Sato, T., Miura, H., Satoh, M., Takayabu, Y. N., & Wang, Y. Q. (2009). Diurnal cycle of precipitation in the tropics simulated in a global cloud-resolving model. *Journal of Climate*, *22*(18), 4809–4826. <https://doi.org/10.1175/2009JCLI2890.1>
- Seo, H. (2017). Distinct influence of air-sea interactions mediated by mesoscale sea surface temperature and surface current in the Arabian Sea. *Journal of Climate*, *30*(20), 8061–8080. <https://doi.org/10.1175/JCLI-D-16-0834.1>
- Seo, H., Subramanian, A. C., Miller, A. J., & Cavanaugh, N. R. (2014). Coupled impacts of the diurnal cycle of sea surface temperature on the Madden-Julian Oscillation. *Journal of Climate*, *27*(22), 8422–8443. <https://doi.org/10.1175/JCLI-D-14-00141.1>
- Shi, R., Chen, J., Guo, X., Zeng, L. L., Li, J., Xie, Q., et al. (2017). Ship observations and numerical simulation of the marine atmospheric boundary layer over the spring oceanic front in the northwestern South China Sea. *Journal of Geophysical Research: Atmospheres*, *122*, 3733–3753. <https://doi.org/10.1002/2016JD026071>
- Shi, R., Guo, X., Wang, D., Zeng, L. L., & Chen, J. (2015). Seasonal variability in coastal fronts and its influence on sea surface wind in the northern South China Sea. *Deep-Sea Research Part II*, *119*, 30–39. <https://doi.org/10.1016/j.dsr.2013.12.018>
- Shu, Y., Wang, D., Zhu, J., & Peng, S. (2011). The 4-D structure of upwelling and Pearl River plume in the northern South China Sea during summer 2008 revealed by a data assimilation model. *Ocean Modelling*, *36*(3–4), 228–241. <https://doi.org/10.1016/j.ocemod.2011.01.002>
- Skamarock, W. C. (2008). A description of the advanced research WRF version 3. *NCAR Technical*, *113*, 7–25.
- Slingo, J., Inness, P., Neale, R., & Woolnough, S. (2003). Scale interactions on diurnal to seasonal timescales and their relevance to model systematic errors. *Annales Geophysicae*, *46*(1), 139–155.
- Small, R. J., Deszoeke, S. P., Xie, S. P., O'Neill, L., Seo, H., Song, Q., et al. (2008). Air–sea interaction over ocean fronts and eddies. *Dynamics of Atmospheres and Oceans*, *45*(3–4), 274–319. <https://doi.org/10.1016/j.dynatmoce.2008.01.001>
- Small, R. J., Tomas, R. A., & Bryan, F. O. (2014). Storm track response to ocean fronts in a global high-resolution climate model. *Climate Dynamics*, *43*(3–4), 805–828. <https://doi.org/10.1007/s00382-013-1980-9>
- Song, Q., Chelton, D. B., Esbensen, S. K., Thum, N., & O'Neill, L. W. (2009). Coupling between sea surface temperature and low-level winds in mesoscale numerical models. *Journal of Climate*, *22*(1), 146–164. <https://doi.org/10.1175/2008JCLI2488.1>
- Su, J., & Pohlmann, T. (2009). Wind and topography influence on an upwelling system at the eastern Hainan coast. *Journal of Geophysical Research*, *114*, C06017. <https://doi.org/10.1029/2008JC005018>
- Su, J., Xu, M., Pohlmann, T., Xu, D., & Wang, D.-R. (2013). A western boundary upwelling system response to recent climate variation (1960–2006). *Continental Shelf Research*, *57*, 3–9. <https://doi.org/10.1016/j.csr.2012.05.010>
- Tanimoto, Y., Xie, S.-P., Kai, K. H., Okajima, H., Tokinaga, H., Murayama, T., et al. (2009). Observations of marine atmospheric boundary layer transitions across the summer Kuroshio Extension. *Journal of Climate*, *22*(6), 1360–1374. <https://doi.org/10.1175/2008JCLI2420.1>
- Tao, W., Huang, G., Wu, R., Hu, K., Wang, P., & Chen, D. (2016). Asymmetry in summertime atmospheric circulation anomalies over the Northwest Pacific during decaying phase of El Niño and La Niña. *Climate Dynamics*, *107*(D19), 2007–2023. <https://doi.org/10.1029/2001JD000393>
- Tiedtke, M. (1989). A comprehensive mass flux scheme for cumulus parameterization in large-scale models. *Monthly Weather Review*, *117*(8), 1779–1800. [https://doi.org/10.1175/1520-0493\(1989\)117<1779:ACMFSF>2.0.CO;2](https://doi.org/10.1175/1520-0493(1989)117<1779:ACMFSF>2.0.CO;2)
- Toy, M. D., & Johnson, R. H. (2014). The influence of an SST front on a heavy rainfall event over coastal Taiwan during TiMREX. *Journal of the Atmospheric Sciences*, *71*(9), 3223–3249. <https://doi.org/10.1175/JAS-D-13-0338.1>
- Vincent, C. L., & Lane, T. P. (2016). Evolution of the diurnal rainfall cycle with the passage of a Madden–Julian Oscillation event through the Maritime Continent. *Monthly Weather Review*, *144*(5), 1983–2005. <https://doi.org/10.1175/MWR-D-15-0326.1>
- Wang, B., Wu, R., & Fu, X. (2000). Pacific–east Asian teleconnection: How does Enso affect east Asian climate? *Journal of Climate*, *13*(9), 1517–1536. [https://doi.org/10.1175/1520-0442\(2000\)013<1517:PEATHD>2.0.CO;2](https://doi.org/10.1175/1520-0442(2000)013<1517:PEATHD>2.0.CO;2)
- Wang, C., & Wang, X. (2013). Classifying El Niño Modoki I and II by different impacts on rainfall in southern China and typhoon tracks. *Journal of Climate*, *26*(4), 1322–1338. <https://doi.org/10.1175/JCLI-D-12-00107.1>
- Wang, D., Liu, Y., Qi, Y., & Shi, P. (2001). Seasonal variability of thermal fronts in the northern South China Sea from satellite data. *Geophysical Research Letters*, *28*(20), 3963–3966. <https://doi.org/10.1029/2001GL013306>
- Wang, D., Shu, Y., Xue, H., Hu, J., Chen, J., Zhuang, W., et al. (2014). Relative contributions of local wind and topography to the coastal upwelling intensity in the northern South China Sea. *Journal of Geophysical Research: Oceans*, *119*, 2550–2567. <https://doi.org/10.1002/2013JC009172>
- Wang, G., Li, J., Wang, C., & Yan, Y. (2012). Interactions among the winter monsoon, ocean eddy and ocean thermal front in the South China Sea. *Journal of Geophysical Research*, *117*, C08002. <https://doi.org/10.1029/2012JC008007>
- Wapler, K., & Lane, T. P. (2012). A case of offshore convective initiation by interacting land breezes near Darwin, Australia. *Meteorology and Atmospheric Physics*, *115*(3–4), 123–137. <https://doi.org/10.1007/s00703-011-0180-6>
- Williams, M., & Houze, A. R. (1987). Satellite-observed characteristics of winter monsoon cloud clusters. *Monthly Weather Review*, *115*(2), 505–519. [https://doi.org/10.1175/1520-0493\(1987\)115<0505:SOCOWM>2.0.CO;2](https://doi.org/10.1175/1520-0493(1987)115<0505:SOCOWM>2.0.CO;2)
- Wu, R., Chen, W., Wang, G., & Hu, K. (2014). Relative contribution of ENSO and East Asian winter monsoon to the South China Sea SST anomalies during ENSO decaying years. *Journal of Geophysical Research: Atmospheres*, *119*, 5046–5064. <https://doi.org/10.1002/2013JD021095>
- Xie, S.-P., Du, Y., Huang, G., Zheng, X.-T., Tokinaga, H., Hu, K., & Liu, Q. (2010). Decadal shift in El Niño influences on indo–western Pacific and East Asian climate in the 1970s. *Journal of Climate*, *23*(12), 3352–3368. <https://doi.org/10.1175/2010JCLI3429.1>
- Xie, S.-P., Hu, K., Hafner, J., Tokinaga, H., Du, Y., Huang, G., & Sampe, T. (2009). Indian Ocean capacitor effect on Indo-Western Pacific climate during the summer following El Niño. *Journal of Climate*, *22*(3), 730–747. <https://doi.org/10.1175/2008JCLI2544.1>
- Xie, S.-P., Xie, Q., Wang, D., & Liu, W. T. (2003). Summer upwelling in the South China Sea and its role in regional climate variations. *Journal of Geophysical Research*, *108*(C8). <https://doi.org/10.1029/2003JC001867>
- Xu, H., Xu, M., Xie, S., & Wang, Y. (2011). Deep atmospheric response to the spring Kuroshio over the East China Sea. *Journal of Climate*, *24*(18), 4959–4972. <https://doi.org/10.1175/JCLI-D-10-05034.1>
- Yamamoto, M. K., Furuzawa, F. A., Higuchi, A., & Nakamura, K. (2008). Comparison of diurnal variations in rainfall systems observed by TRMM PR, TMI, and VIRS. *Journal of Climate*, *21*(16), 4011–4028. <https://doi.org/10.1175/2007JCLI2079.1>
- Yang, G., & Slingo, J. M. (2001). The diurnal cycle in the tropics. *Monthly Weather Review*, *129*(4), 784–801. [https://doi.org/10.1175/1520-0493\(2001\)129<0784:TDCITT>2.0.CO;2](https://doi.org/10.1175/1520-0493(2001)129<0784:TDCITT>2.0.CO;2)
- Yokoi, S., Mori, S., Katsumata, M., Geng, B., Yasunaga, K., Syamsudin, F., et al. (2017). Diurnal cycle of precipitation observed in the western coastal area of Sumatra island: Offshore preconditioning by gravity waves. *Monthly Weather Review*, *145*(9), 3745–3761. <https://doi.org/10.1175/MWR-D-16-0468.1>

- Zhang, C., Wang, Y., & Hamilton, K. (2011). Improved representation of boundary layer clouds over the Southeast Pacific in ARW-WRF using a modified Tiedtke cumulus parameterization scheme. *Monthly Weather Review*, *139*(11), 3489–3513. <https://doi.org/10.1175/MWR-D-10-05091.1>
- Zhang, R. H., Min, Q. Y., & Su, J. Z. (2017). Impact of El Niño on atmospheric circulations over East Asia and rainfall in China: Role of the anomalous western North Pacific anticyclone. *Science China Earth Sciences*, *60*(6), 1124–1132. <https://doi.org/10.1007/s11430-016-9026-x>
- Zipser, E. J. (1977). Mesoscale and convective-scale downdrafts as distinct components of squall-line structure. *Monthly Weather Review*, *105*(12), 1568–1589. [https://doi.org/10.1175/1520-0493\(1977\)105<1568:MACDAD>2.0.CO;2](https://doi.org/10.1175/1520-0493(1977)105<1568:MACDAD>2.0.CO;2)